

Annual Review of Materials Research

Spontaneous Ordering of Oxide-Oxide Epitaxial Vertically Aligned Nanocomposite Thin Films

Xing Sun,¹ Judith L. MacManus-Driscoll,²
and Haiyan Wang^{1,3}

¹School of Materials Engineering, Purdue University, West Lafayette, Indiana 47907, USA;
email: sun654@purdue.edu, hwang00@purdue.edu

²Department of Materials Science and Metallurgy, University of Cambridge, Cambridge CB3
OFS, United Kingdom; email: jld35@cam.ac.uk

³School of Electrical and Computer Engineering, Purdue University, West Lafayette,
Indiana 47907, USA

Annu. Rev. Mater. Res. 2020. 50:229–53

First published as a Review in Advance on
May 13, 2020

The *Annual Review of Materials Research* is online at
matsci.annualreviews.org

<https://doi.org/10.1146/annurev-matsci-091719-112806>

Copyright © 2020 by Annual Reviews.
All rights reserved

Keywords

spontaneous ordering, vertically aligned nanocomposites, thermodynamics, kinetics, oxide-oxide

Abstract

The emerging field of self-assembled vertically aligned nanocomposite (VAN) thin films effectively enables strain, interface, and microstructure engineering as well as (multi)functional improvements in electric, magnetic, optical, and energy-related properties. Well-ordered or patterned microstructures not only empower VAN thin films with many new functionalities but also enable VAN thin films to be used in nanoscale devices. Comparative ordered devices formed via templating methods suffer from critical drawbacks of processing complexity and potential contamination. Therefore, VAN thin films with spontaneous ordering stand out and display many appealing features for next-generation technological devices, such as electronics, optoelectronics, ultrahigh-density memory systems, photonics, and 3D microbatteries. The spontaneous ordering described in this review contains ordered/patterned structures in both in-plane and out-of-plane directions. In particular, approaches to obtaining spontaneously ordered/patterned structures in-plane are systematically reviewed

**ANNUAL
REVIEWS CONNECT**

www.annualreviews.org

- Download figures
- Navigate cited references
- Keyword search
- Explore related articles
- Share via email or social media

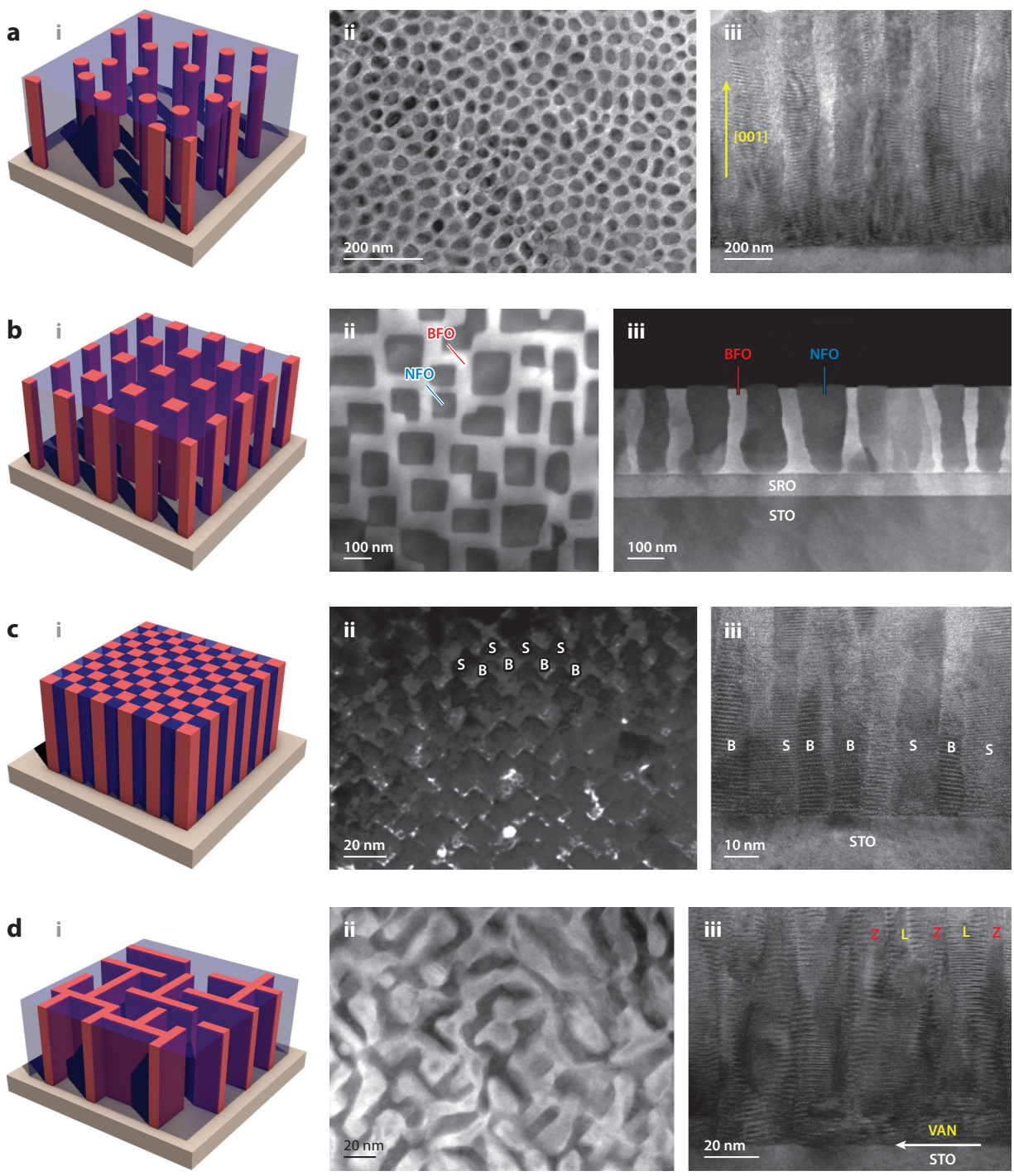
from both thermodynamic and kinetic perspectives. Out-of-plane ordering is also discussed in detail. In addition to reviewing the progress of VAN films with spontaneous ordering, this article also highlights some recent developments in spontaneous ordering approaches and proposes future directions.

1. INTRODUCTION

Extensive efforts and studies have been devoted to achieving next-generation technological devices—aiming for small, smart, and powerful. Compared with their bulk form counterparts, thin films are more suitable for practical device integration. Complex oxide thin films offer a wide range of tunable properties for functional devices, especially for energy and information technologies, exploiting semiconducting, magnetic, optical (including plasmonic), mechanical, and catalytic properties (1–6).

Recently, heteroepitaxial nanocomposite thin films have been recognized as ideal systems for multifunctional devices, bridging the gap between conventional functional devices and nanoscale ones (7). The type of microstructures of nanocomposite thin films largely depends on interfacial energy balances (for the interfaces between the two film phases and the substrate and the interfaces between the two film phases themselves) and the kinetics. The microstructures of nanocomposite thin films are randomly arranged composite structures that range from the 0–3 configuration (nanoparticles embedded in a matrix) to the 1–3 configuration, in the form of vertically aligned nanocomposites (VANs) (8–15). In VAN thin films, two immiscible phases simultaneously grow on a given substrate and form vertical interfaces and columnar microstructures. Compared with conventional thin films, VAN microstructures can enable vertical strain engineering within the films due to their very large vertical interface area, allowing them to overcome the limitations of critical film thickness (16). Interfacial coupling between the materials in the VAN films, the nature of the interfaces formed between them, and the strain induced in the phase all have profound influences on the performance of the films (8, 12, 14, 17). Consequently, VAN films achieve markedly improved physical properties in, e.g., ferroelectrics, ferromagnetics, multiferroics, superconductors, piezoelectrics, and ionics (11–14). The growth mechanisms behind the formation of VAN films have been discussed in earlier reviews (12, 18), including the thermodynamics (balance between interfacial energy terms and the strain energy terms) behind the formation of the random VAN microstructures (18) and the origin of ordered VAN microstructures that form from spinodal decomposition (12). However, the origin of ordered microstructures that are not formed by spinodal or pseudospinodal decomposition has not been covered previously, as these microstructures have only been observed recently. In this article, we focus more on understanding the fascinating recent observations of lateral ordering and the combined lateral and vertical spontaneous ordering in VAN oxide films. We review the contributions that thermodynamics, kinetics, and self-templated growth play in achieving ordered structures.

As shown in **Figure 1**, VAN films have achieved distinct microstructures where size, shape, orientation, and distribution of the nanodomains can be readily tuned, including circular nanopillars-in-matrix, rectangular nanopillars-in-matrix, nanocheckerboard, and nanomazes (8, 10, 11, 13, 17–32). Among the various morphologies, VAN thin films with ordered/patterned structures have drawn tremendous interest from nanoscience and nanotechnology fields, since they not only benefit the miniaturization and integration of the multifunctional devices but also enable unprecedented properties compared to their random counterparts.



(Caption appears on following page)

Figure 1 (Figure appears on preceding page)

(*a, i*) A 3D schematic illustration and (*ii*) plan-view and (*iii*) cross-sectional TEM images of a BTO-SmO VAN microstructure with circular SmO nanopillars embedded in a BTO matrix. (*b, i*) A 3D schematic illustration and (*ii*) plan-view and (*iii*) cross-sectional STEM images of a BFO-NFO VAN microstructure with rectangular/square NFO nanopillars embedded in a BFO matrix. (*c, i*) A 3D schematic illustration and (*ii*) plan-view and (*iii*) cross-sectional TEM images of a BFO-SmO VAN thin film with a nanocheckerboard microstructure. (*d, i*) A 3D schematic illustration and (*ii*) plan-view STEM and (*iii*) cross-sectional TEM images of an $\text{La}_{0.7}\text{Sr}_{0.3}\text{MnO}_3\text{-ZnO}$ VAN film with a nanomaze microstructure. Abbreviations: BFO, BiFeO_3 ; BTO, BaTiO_3 ; L, $\text{La}_{0.7}\text{Sr}_{0.3}\text{MnO}_3$; NFO, NiFe_2O_4 ; SmO, Sm_2O_3 ; STEM, scanning transmission electron microscopy; STO, SrTiO_3 ; SRO, SrRuO_3 ; TEM, transmission electron microscopy; VAN, vertically aligned nanocomposite; Z, ZnO. Panel *a* adapted with permission from Reference 19, panel *b* adapted with permission from Reference 20, panel *c* adapted with permission from Reference 17, and panel *d* adapted with permission from Reference 21.

Many unique functionalities in nature, such as the self-cleaning ability of lotus leaves, the dry adhesive force of gecko feet, and color change in chameleons, are closely attributed to ordered/patterned structures from macroscale to nanoscale (33–37). For example, as shown in **Figure 2**, the active color change ability of chameleons is derived from the ordered arrangement of its functional blocks of guanine nanocrystals packed under the epidermis (37). A chameleon has two layers of dermal iridophore cells. The superficial iridophores in the upper layer have guanine nanocrystals packed in an ordered pattern. In the relaxed condition, the functional guanine nanocrystals are closely packed with small spacing (**Figure 2a, subpanel i**) and the photonic effect reflects blue light. The chameleon shows a green color overall when the blue light is combined with the layer of epidermis with chromatophores containing yellow pigments (**Figure 2b, subpanel i**). However, when the chameleon is excited, the spacing between ordered functional guanine nanocrystals is highly expanded (**Figure 2a, subpanel ii**), producing a color shift from green to yellow (**Figure 2b, subpanel ii**). Therefore, the spatial arrangement of the functional blocks can directly tune the ultimate color change performance of the chameleon (36, 37).

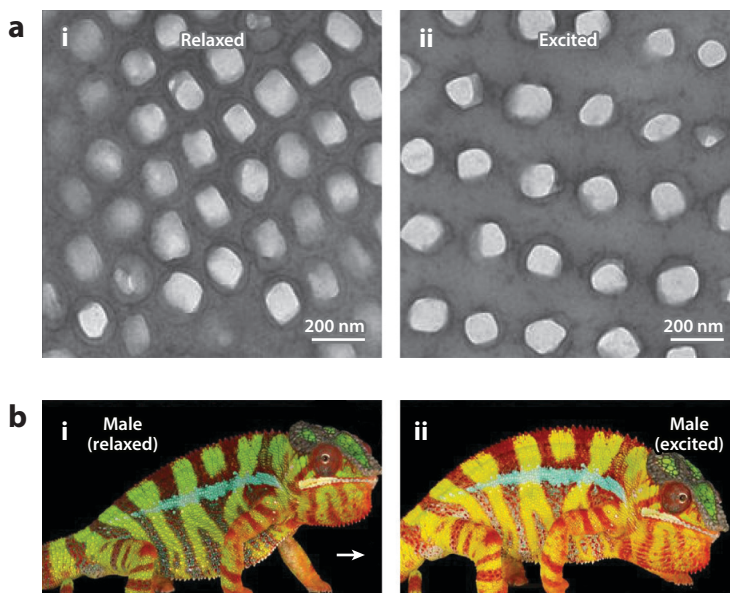


Figure 2

Transmission electron microscopy images of the ordered guanine nanocrystals in the superficial iridophores at the (*a, i*) relaxed and (*a, ii*) excited conditions of a chameleon corresponding to the color change from (*b, i*) green (at its relaxed state) to (*b, ii*) yellow (at its excited state). Figure adapted with permission from Reference 37.

Inspired by nature, researchers have artificially fabricated ordered structures across different scales and obtained intriguing multifunctionalities, both in functional and structural applications (33, 36, 38–42). As mentioned, the ordered microstructures of VAN films can fully utilize the limited space and achieve higher working efficiencies, with benefits to small-scale technological device integration and fabrication (43–49). The nanopillars or nanodomains of the secondary phase in the ordered VAN microstructures are arranged in a specific well-defined pattern with regularity or periodicity along the in-plane direction, such as the nanocheckerboard microstructure in **Figure 1c, subpanel ii**; in contrast, in more standard random VAN films, there is no ordering of nanopillars or nanodomains along the in-plane direction. There are two main strategies for achieving ordered/patterned structures in VAN films: templated growth and spontaneously ordered growth. Templated growth mainly includes use of anodic aluminum oxide, polymers, colloidal templates, focused ion beams, and photolithography (6, 46, 47, 49–53). Templated growth is quite feasible and versatile in a wide range of composite systems with typical geometric features ranging from several micrometers to hundreds of nanometers. As an alternative approach, this spontaneous ordering can exhibit precise pattern registration by careful and rational deposition control. More importantly, the spontaneously ordered growth is able to overcome some limitations of the templated growth. For example, the domain dimensions during spontaneous ordering can be scaled down to several nanometers. The spontaneously ordered growth process occurs naturally, hence providing a simple, clean, low-cost, and convenient system without the complications of external template removal. The process can efficiently minimize defects and avoid the unexpected damage derived from templated growth (7). Accordingly, spontaneous ordering is more suitable for fulfilling the requirements of small-scale technological device integration, such as 3D micro- and nanobattery design with a minimized volume of electrolytes, ultrahigh density resistive and magnetoelectric memory, lab-on-a-chip, photonics, and more high-tech fields (36, 54–64).

It has been noted that the heteroepitaxial nanocomposite films reported are mostly obtained through pulsed laser deposition (PLD) with one composite target or multiple single-phase targets simultaneously in the high vacuum chamber, but there are also reports of growth by molecular beam epitaxy, sputtering, chemical solution deposition, and other techniques (4, 65–71). The examples given in this review are mainly PLD-grown systems, which most reports have adopted. The strategies and related principles are also applicable for nanocomposite films fabricated by other synthesis methods.

2. IN-PLANE SPONTANEOUS ORDERING

In most reports, nanopillars or nanodomains are randomly distributed in the matrix of VAN films due to the complex deposition and diffusion process (72). Hence, for nanoscale devices it remains an unsolved challenge to fabricate spontaneously ordered/patterned nanostructures in continuous films. Indeed, there are few reports regarding purposeful spontaneous ordering or controllable patterned arrangement in VAN systems (11, 13, 17, 19, 64, 73–75). For in-plane spontaneous ordering within VAN systems, the major approaches summarized in this review are discussed from the following aspects (**Figure 3**) (13, 75–77): surface/interface energy (Section 2.1), strain energy (including Sections 2.1, 2.2, and 2.3), growth kinetics (Section 2.4), and self-templated growth (Section 2.5).

2.1. Substrate Orientation and Influence on In-Plane Ordering

Spontaneously ordered growth is a self-assembled process without involvement of external forces, and the driving force is minimization of free energy in the system. The first energy term to consider is surface/interface energy, which plays a significant role in determining the crystal

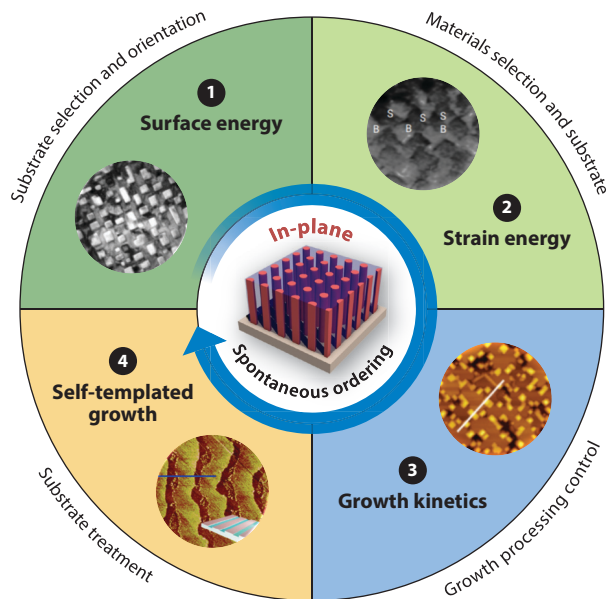


Figure 3

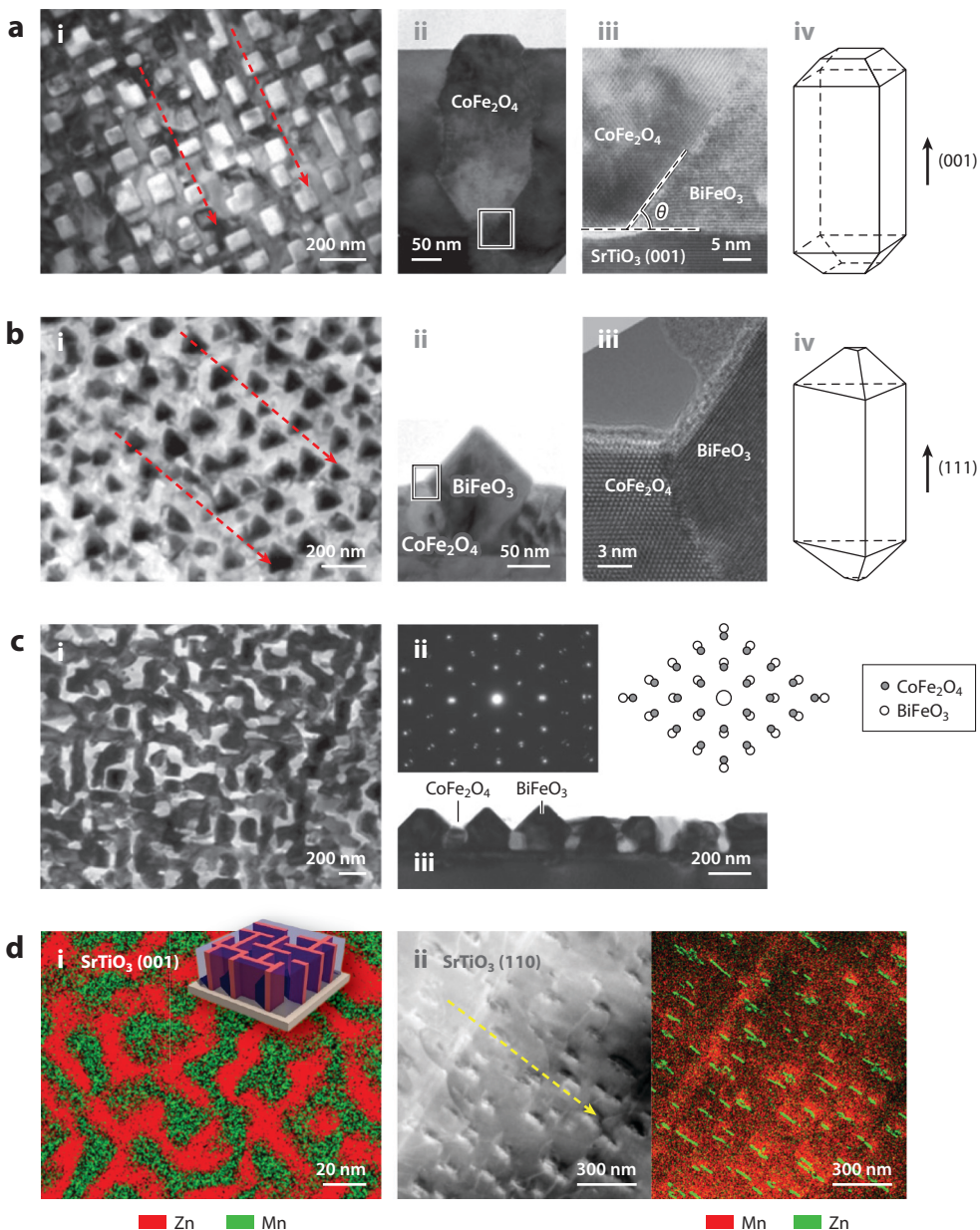
Schematic of the reviewed strategies to achieve in-plane spontaneously ordered nanostructures in vertically aligned nanocomposite thin films. ❶ Surface/interface energy strategy by controlling substrate selection and orientation, ❷ strain energy strategy by rationally selecting the film and substrate materials (B is BiFeO₃ and S is Sm₂O₃), ❸ growth kinetics strategy by controlling the growth processing parameters, and ❹ self-templated growth strategy via substrate treatment. ❶ Adapted with permission from Reference 75, ❷ adapted with permission from Reference 13, ❸ adapted with permission from Reference 76, and ❹ adapted with permission from Reference 77.

nucleation and growth process as well as the ultimate microstructure, including size and shape of nanodomains. The surface/interface energies are sensitive to the substrate orientation, as the different crystallographic orientations of the substrates enable quite distinct surface/interface energies due to the atomic arrangement (64, 78–80).

Much work has been focused on the influence of substrate orientation on heteroepitaxial VAN films and tunable microstructures with spontaneous ordering (64, 74–76, 81–83). For example, the microstructure evolution of the perovskite-spinel BiFeO₃ (BFO)–CoFe₂O₄ (CFO) VAN system was studied on different substrate orientations (**Figure 4**) (64, 75). Due to the different surface energy anisotropy between the perovskite and spinel phases, in VAN thin films the role of each phase as matrix and pillar can be reversed when grown on differently oriented SrTiO₃ (STO) substrates. As the growth was accomplished by one-step PLD using one BFO-CFO composite target, BFO and CFO adatoms are simultaneously ablated and deposited, forming vertical interfaces. BFO (001) has a much lower surface energy than that of STO (001); thus, BFO (001) fully wets the STO substrate surface as the film matrix. CFO (001) has a higher surface energy than that of STO (001) and only partially wets the substrate and forms the nanopillars (**Figure 4a, subpanels i–iv**). In contrast, on STO (111) substrates, it was reported that CFO (111) exhibits the lowest surface energy in the system and is energetically favorable as the matrix, while BFO (111) grows into triangular nanopillars in the CFO matrix (**Figure 4b, subpanels i–iv**). Along the (110) orientation, BFO and CFO exhibit similar surface energies and form a nanomaze microstructure (**Figure 4c, subpanels i–iii**). In this case, the matrix-pillar roles depend on the relative amounts

of the two phases (64, 74, 75, 84). This work suggests that the surface/interface energy plays an important role in the overall morphology of VAN films, including pillar-matrix roles and shapes of nanodomains (20, 64, 81).

The obvious phase separation with clear interfaces corresponds to a well-defined microstructure, which is an important prerequisite for the spontaneously ordered spatial arrangement of nanodomains and could also be enabled by strain energy minimization. As shown in **Figure 4a**, **subpanel i**, and **b**, **subpanel i**, the pillar domains are in-plane aligned along certain well-defined



(Caption appears on following page)

Figure 4 (Figure appears on preceding page)

(*a, i*) Plan-view and (*ii*) cross-sectional TEM images of a BiFeO₃-CoFe₂O₄ VAN film grown on SrTiO₃ (001) substrate. (*iii*) HRTEM image of the interface area marked by the rectangle in subpanel *ii*. (*iv*) Schematic illustration showing the growth of a CoFe₂O₄ nanopillar on an SrTiO₃ (001) substrate. (*b, i*) Plan-view and (*ii*) cross-sectional TEM images of a BiFeO₃-CoFe₂O₄ VAN film grown on an SrTiO₃ (111) substrate. (*iii*) HRTEM image of the interface area marked by the rectangle in subpanel *ii*. (*iv*) Schematic illustration showing a BiFeO₃ nanopillar on an SrTiO₃ (111) substrate. (*c, i*) Plan-view TEM, (*ii*) the corresponding SAED, and (*iii*) cross-sectional TEM images of a BiFeO₃-CoFe₂O₄ VAN film grown on an SrTiO₃ (110) substrate. Panels *a-c* adapted with permission from Reference 75. (*d, i*) Plan-view EDS mapping of an LSMO-ZnO VAN thin film grown on an SrTiO₃ (001) substrate, exhibiting nanomaze microstructure. (*ii*) Plan-view STEM and corresponding EDS mapping images of an LSMO-ZnO VAN thin film grown on an SrTiO₃ (110) substrate. Panel *d* subpanel *i* adapted with permission from Reference 21. Abbreviations: EDS, energy-dispersive X-ray spectroscopy; HRTEM, high-resolution transmission electron microscopy; LSMO, La_{0.7}Sr_{0.3}MnO₃; SAED, selected area electron diffraction; STEM, scanning transmission electron microscopy; TEM, transmission electron microscopy; VAN, vertically aligned nanocomposite.

directions and exhibit spatial registration on STO (001) and (111) substrates. Similar scenarios have been reported in other perovskite-spinel composite films (e.g., PbTiO₃-CoFe₂O₄) as well. The in-plane periodic and ordered arrangement of the nanopillars is attributed to the formation of dislocations for relaxing the strain from lattice mismatching (64, 72, 85, 86). In these cases, the perovskite and spinel phases are both estimated under large compressive strain in-plane after the initial coherent growth on STO substrates (86, 87). To relax strain and minimize the system energy, dislocations are generated and distributed in a highly ordered periodic pattern. The mutual repulsion between each dislocation helps to enable good registration and ordered distribution in the pattern (61, 88). Meanwhile, the dislocations also guide the adatoms' diffusion on the surface via repulsive or attractive forces and pass the ordered periodicity down to the pillar domains as templates through nucleation of pillar domains. The strain relief patterned dislocations have been widely employed to fabricate spontaneously ordered arrays of metal and semiconductor nanostructures with long-range periodicity (59, 61, 72, 85, 89, 90). Therefore, it is a strain-driven effect that the pillar domains are lined up and display the ordered patterns with high registry, regularity, and periodicity in the perovskite-spinel VAN films.

Besides perovskite-spinel systems, this review also presents an example of a perovskite-wurtzite system, La_{0.7}Sr_{0.3}MnO₃ (LSMO)-ZnO VANs on STO (001) and (110) substrates, confirming that the effect of substrate orientation on spontaneous ordering is also applicable to different crystal systems. LSMO-ZnO VAN thin films exhibit a nanomaze-like microstructure on STO (001) substrates with ZnO nanodomains interconnected and randomly distributed in an LSMO matrix (**Figure 4d, subpanel i**) (21). However, when grown on STO (110) substrates (**Figure 4d, subpanel ii**), all of the ZnO nanodomains become elongated, rectangular nanopillars uniformly arranged in the LSMO matrix. More importantly, the ZnO rectangular nanopillars are well aligned with the longer edges parallel along the <100> direction when grown on an STO (110) substrate (**Figure 4d, subpanel ii**). Such tuning of domain morphology and alignment is due not only to the different surface energies on the STO (110) surface but also to the different elastic strain effect between the film and the substrate, which drives the rectangular nanodomain formation and alignment to minimize the overall energy (80, 82, 86, 91). For those cubic systems that are isotropic, the lattice mismatch and strain do not vary significantly as a function of the substrate orientation; however, for anisotropic systems such as hexagonal close packed, both the lattice mismatch and strain may vary as a function of the substrate orientation.

Therefore, the substrate orientation not only enables tuning of the microstructure but it also can be used as an effective tool to achieve spontaneous ordering in VAN films of diverse

composite systems. Here, the spontaneously ordered/patterned microstructure is determined by the synergistic effect between the surface/interface energy and the strain energy.

2.2. Substrate Strain and Influence on In-Plane Ordering

As discussed in Section 2.1, the surface/interface energy terms dominate the growth behavior and ultimate microstructure of the VAN films, and the ordered arrangement of those nanodomains is mainly governed by the dislocation patterns that form to provide strain relaxation. Since the strain is generated from lattice mismatch between the film and the substrate, this section focuses on the influence of the different in-plane strain values due to the application of different substrates and highlights the significance of strain on the spatial arrangement of nanodomains.

Strain engineering has been extensively studied on single-phase epitaxial films by using different substrates with distinct lattice parameters (92), but only a few reports have explored the effect of substrate selection on VAN films (26, 93–97). The crystal structure of the BFO matrix was observed to evolve from tetragonal to rhombohedral BFO and then decomposition in BFO-CFO VAN films by simply using different substrates [e.g., LaAlO_3 (LAO), LaNiO_3 (LNO), STO, MgAl_2O_4 , and MgO] of the same orientation but a gradually increasing lattice parameter from 3.79 to 4.21 Å (**Figure 5a**) (94). The lattice distortion and phase transition are caused by strain energy minimization. Although minor size variations of CFO nanopillars are observed on different substrates (**Figure 5b**), the ordered patterns of the nanopillars are still similar to those in **Figure 4a, subpanel i**. Just as for substrate orientation (see Section 2.1), ordered spatial arrangement of nanodomains is also driven by strain relaxation effects, as long as the two VAN phases are both under the same type of strain (compression or tension) and the strain field is uniform across the substrate surface.

The BFO-CFO VAN film grown on LAO presents a better-defined ordering of CFO nanopillars compared with the films on LNO and STO substrates (**Figure 5b**). This is associated with the opposite strain states of BFO and CFO phases, i.e., the in-plane strains of BFO and CFO are estimated to be in tension ($\sim 3.55\%$) and compression (-9.76%) on the LAO substrate, respectively, while on LNO and STO substrates they are both under compressive strain. This effect will be discussed in detail in Section 2.3.

2.3. Strain Compensation Model for In-Plane Ordering

Many VAN films have been reviewed (**Supplemental Figure 1**), and the ones with spontaneous ordering are summarized in **Figure 6a** (7, 8, 11, 13, 17, 19, 20, 64, 73, 81, 97–103). The left and right axes represent the lattice parameters of phases A and B, respectively. The reported A-B VAN films with spontaneous ordering are indicated, along with the typical substrates, including MgO , MgAl_2O_4 , STO, LNO, LAO, and $\text{Zr}_{0.92}\text{Y}_{0.08}\text{O}_{1.96}$ (YSZ). According to the discussion in Sections 2.1 and 2.2, two types of VAN films demonstrate in-plane spontaneously ordered microstructures. One type is BFO-CFO VAN films grown on STO substrates, where both film phases are under compression (or in tension) and spontaneous ordering can be achieved by strain relaxation. In this type of VAN films, the VAN film data are above (or below) that of the substrates in **Figure 6a**. However, some of the data for the A-B VAN films cross that of their substrates, suggesting that the A and B phases are under the opposite strain states, i.e., compression and tension, grown on the substrates. These A-B VAN films can exhibit well-defined ordered microstructure spontaneously, i.e., either pillar-in-matrix or nanocheckerboard structures. The intersections between the data are indicated in **Figure 6a**, predicting the molar fraction of B with ideal strain compensation.

Supplemental Material >

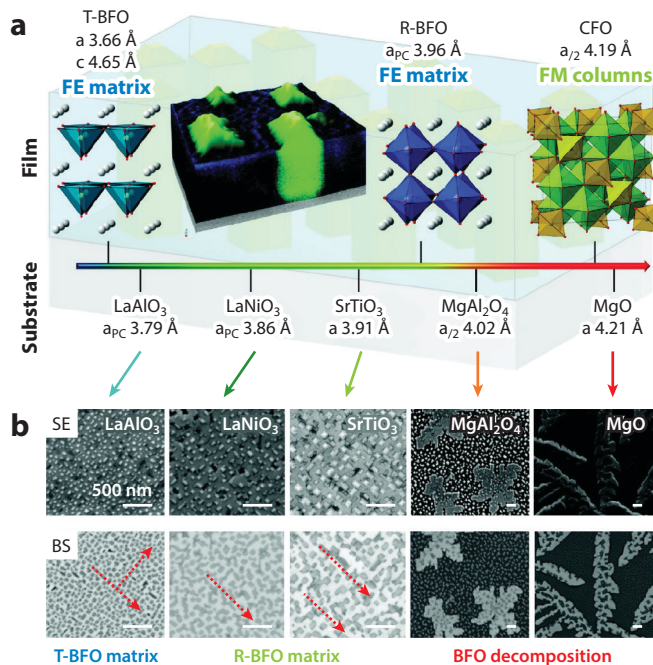
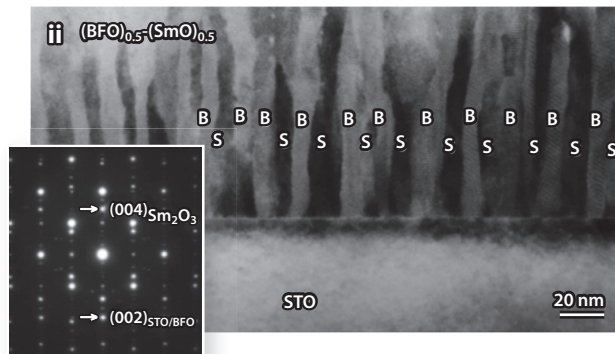
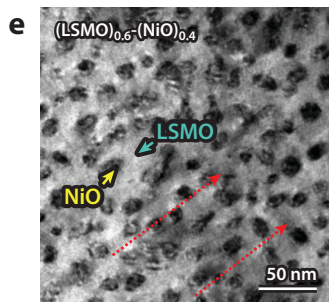
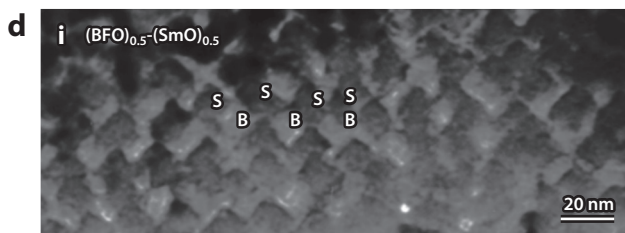
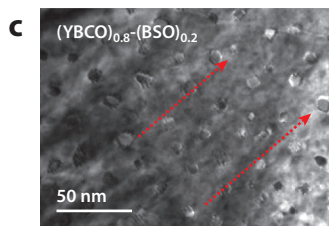
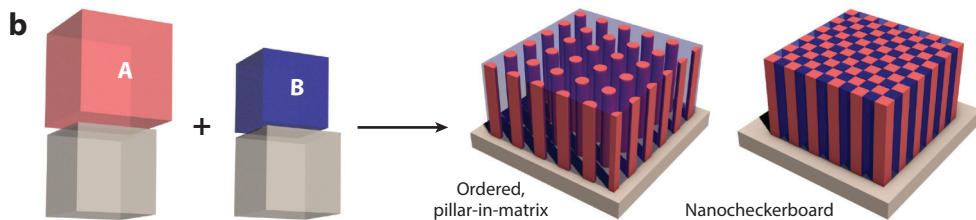
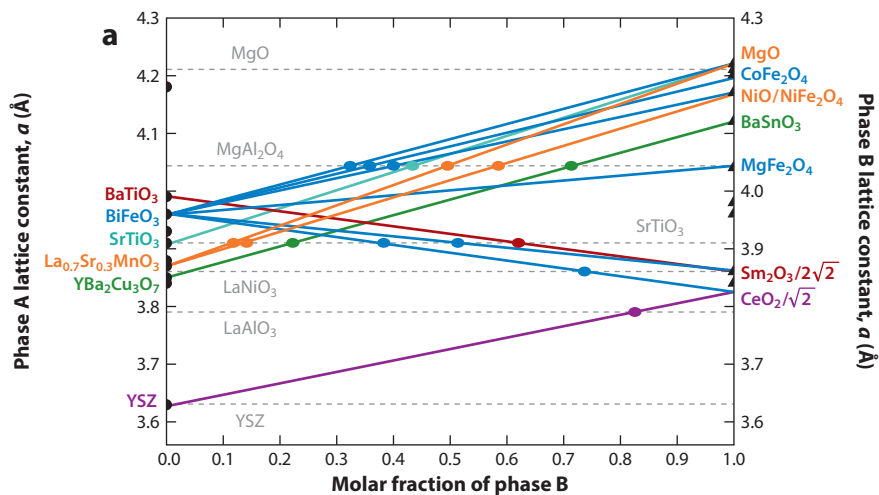


Figure 5

(a) Schematic illustration showing the crystal structures of tetragonal BiFeO_3 (T-BFO), rhombohedral BiFeO_3 (R-BFO), and CoFe_2O_4 (CFO) and the lattice evolution of the substrates (i.e., LaAlO_3 , LaNiO_3 , SrTiO_3 , MgAl_2O_4 , and MgO). The letters a and c represent the lattice parameters along lateral and vertical directions, respectively, a_2 represents half of the corresponding lattice parameter, and a_{PC} corresponds to the pseudocubic lattice of R-BFO since it can be described as a distorted perovskite cell. (b) Scanning secondary electron (SE) and backscattered electron (BS) images of BFO-CFO vertically aligned nanocomposite films grown under similar conditions but on different substrates, showing the in-plane microstructural evolution driven by the substrates (scale bars: 500 nm). Abbreviations: FE, ferroelectric; FM, ferromagnetic. Figure adapted with permission from Reference 94.

To explain the second type of in-plane spontaneous ordering, we propose a strain compensation model (**Figure 6b**) in which the lattice parameter of the substrate is between that of the A and B phases in the A-B VAN film. Accordingly, the A and B domains are supposed to be in compression and tension in-plane, respectively. After self-assembling into an A-B VAN film, minimization of the strain energy leads to alternately arranged A and B domains located next to each other across the entire film. This strain compensation effect generates the highly ordered microstructure as shown in **Figure 6b**. For example, after coupling with STO (001) substrate ($a_{\text{STO}} = 3.91 \text{ \AA}$), $\text{YBa}_2\text{Cu}_3\text{O}_7$ (YBCO; $a_{\text{YBCO}} = 3.85 \text{ \AA}$) and BaSnO_3 (BSO; $a_{\text{BSO}} = 4.12 \text{ \AA}$) are estimated to be under in-plane strains of $\sim 1.43\%$ (tensile) and $\sim -5.22\%$ (compressive), respectively (11). Since the relative molar ratio of the two phases is 4:1, the YBCO and BSO phases in the $(\text{YBCO})_{0.8}\text{-(BSO)}_{0.2}$ VAN film are preferred under tensile and compressive strains with similar accumulated strains of 1.14% for YBCO and -1.04% for BSO. The strain compensation effect leads to the highly ordered pillar-in-matrix microstructure of $(\text{YBCO})_{0.8}\text{-(BSO)}_{0.2}$ VAN film for energy minimization (**Figure 6c**) (11). In addition, BFO ($a_{\text{BFO}} = 3.96 \text{ \AA}$) and Sm_2O_3 (SmO ; $a_{\text{SmO}} \times \sqrt{2}/4 = 3.86 \text{ \AA}$) are calculated to be under in-plane strains of -1.44% (compressive) and 1.17% (tensile), respectively, when grown on STO (001) substrate (13, 17). With a relative ratio of 1:1, BFO-SmO VAN films



(Caption appears on following page)

Figure 6 (Figure appears on preceding page)

(a) Theoretical in-plane lattice matching distances as a function of the relative molar ratio between A and B in VAN thin films. The left axis is for phase A, and the right axis is for phase B. The colored lines connecting phases A and B mark the A-B VAN films with spontaneously ordered microstructures. The dashed gray lines represent the in-plane lattice parameters of the typical substrates, e.g., MgO, MgAl₂O₄, STO, LaNiO₃, LaAlO₃, and YSZ (7, 8, 11, 13, 17, 19, 20, 64, 73, 81, 97–103). (b) Schematic diagram of the in-plane strain compensation model leading to ordered pillar-in-matrix or nanocheckerboard microstructures. (c) Plan-view TEM image of a YBCO-BSO VAN thin film. (d, i) Plan-view and (ii) cross-sectional TEM images of a BFO-SmO VAN thin film grown on an STO substrate with the corresponding selected-area diffraction pattern in the inset of panel d, subpanel ii. (e) Plan-view TEM image of an LSMO-NiO VAN thin film grown on an STO substrate. Abbreviations: BFO, BiFeO₃; BSO, BaSnO₃; STO, SrTiO₃; TEM, transmission electron microscopy; VAN, vertically aligned nanocomposite; YBCO, YBa₂Cu₃O₇; YSZ, Zr_{0.92}Y_{0.08}O_{1.96}. Panel c adapted with permission from Reference 11, panel d adapted with permission from Reference 13, and panel e adapted with permission from Reference 73.

exhibit an excellent nanocheckerboard microstructure (**Figure 6d**, subpanel i) (13). The VAN films tend to demonstrate a spontaneously ordered pattern as long as the two phases are under opposite strain states (i.e., compressive and tensile) compared with the bulk values (12). Actually, even if the relative ratio of BFO and SmO is changed and the strain values are not uniform, the VAN films still can maintain a well-ordered microstructure (11). Similarly, the calculated in-plane strains of LSMO and NiO domains are 0.54% (tensile) and -2.54% (compressive), respectively, in (LSMO)_{0.6}-(NiO)_{0.4} VAN films on STO (001) substrates, where NiO nanopillars are still aligned and distributed in an ordered fashion (**Figure 6e**) (73). The driving force of the strain compensation effect is also the strain energy minimization.

In addition to oxide-oxide systems, strain compensation-induced spontaneous ordering was observed in nitride-metal systems such as TaN-Au VAN films (104). After the system was coherently grown on MgO ($a_{\text{MgO}} = 4.212 \text{ \AA}$) substrate, TaN ($a_{\text{TaN}} = 4.370 \text{ \AA}$) was estimated to be under a compressive strain of $\sim -3.68\%$ in-plane and Au ($a_{\text{Au}} = 4.065 \text{ \AA}$) was estimated to be under a tensile strain of $\sim 3.55\%$ in-plane. The opposite strain states with similar strain values drive the Au nanopillars to align in an ordered hexagonal closely packed fashion embedded in the TaN matrix to minimize the elastic strain energy of the entire system (**Supplemental Figure 2a**). Under the opposite strain states even with different strain values, the Au nanopillars still lined up parallel to a certain direction in the TiN matrix grown on the MgO substrate (**Supplemental Figure 2b**) (104). Overall, elastic strain energy plays a dominant and profound role in self-assembled nanostructures with spontaneous ordering (91, 105, 106).

2.4. Growth Condition (Kinetic) Control

Strain energy is important for determining the ordered/patterned spatial arrangement of nanodomains in VAN thin films, which has been emphasized in Sections 2.1, 2.2, and 2.3. Although spontaneous ordering is energetically dominant, rational kinetic control is an essential prerequisite to enable the ordered/patterned epitaxial microstructures and to tune the nanodomain spacing (12, 13, 59, 66, 76, 107). In this section, using the PLD-grown VAN systems as examples, we discuss the major effects of kinetic growth parameters on PLD growth, including deposition temperature and oxygen pressure.

Among the growth control parameters of PLD, the deposition temperature is a common way to tailor the morphology, stoichiometry, strain state, and interfacial coupling in VAN thin films (11, 76). The lateral width of the nanopillars in BFO-CFO VAN thin films increases with higher deposition temperature, as expected, even on differently oriented substrates (**Figure 7a**) (76). Actually, as long as the VAN thin film growth is a diffusion-controlled process, the temperature dependence

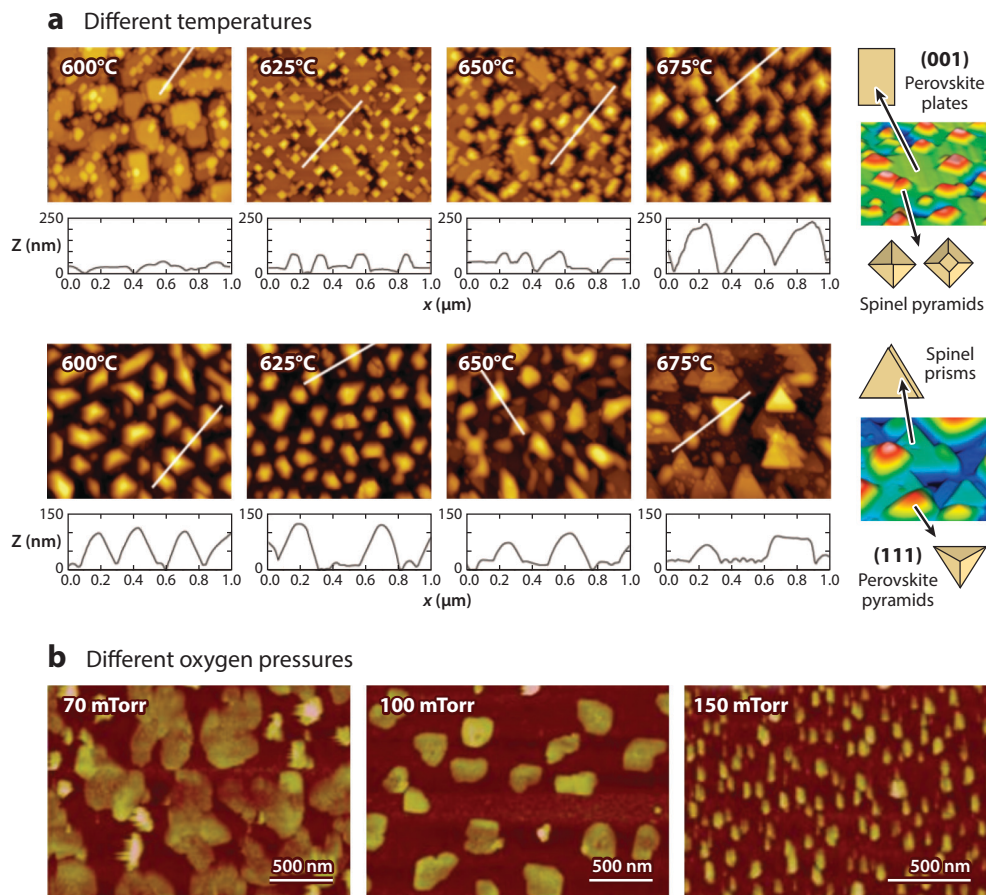


Figure 7

(a) AFM topographic images of BFO-CFO VAN films on STO (001) (*top row*) and STO (111) (*bottom row*) deposited under different temperatures. The white line in each image indicates the line scan direction of the corresponding height profile underneath, where the vertical axis corresponds to the height in nanometers. (b) AFM topographic images of CeO₂-BFO VAN thin films prepared under different oxygen pressures. Abbreviations: AFM, atomic force microscopy; BFO, BiFeO₃; CFO, CoFe₂O₄; STO, SrTiO₃; VAN, vertically aligned nanocomposite. Panel *a* adapted with permission from Reference 76, and panel *b* adapted with permission from Reference 7.

of the nanostructure follows an Arrhenius behavior, as expressed by the following equation (15, 75, 108–110):

$$d^2 = \left(4D_0 e^{\frac{-E_a}{kT}}\right) \frac{1}{v}, \quad 1.$$

where d is the nanopillar width, D_0 is the surface diffusion constant, v is the growth rate (in the thickness direction), E_a is the activation energy for surface diffusion, k is Boltzmann's constant, and T is the absolute temperature. Overall, when the growth rate v is constant, the pillar size $\ln(d)$ is proportional to the deposition temperature T ; when the deposition T is constant, the pillar size d^2 is inversely proportional to the growth rate v . Increasing deposition temperature directly boosts the diffusion kinetics, resulting in larger nanodomains, lower nanodomain density in the matrix,

and better alignment of the domains (**Figure 7a**) (76). Similar phenomena were also observed in previous reports (81, 111). Sufficient kinetic energy helps adatoms travel to their energetically favorable locations in order to reduce the total free energy of the system. Therefore, the deposition temperature can be used to adjust the feature size, spacing, and arrangement of the nanostructures. Besides oxide-oxide systems, the relation also works well in different types of composite systems, such as oxide-metal nanocomposite films (75, 108, 109, 112).

In addition to the deposition temperature, the working pressure during PLD is directly associated with the film growth rate and can also efficiently tune the morphology and alignment of the pillar domains. For example, when the working pressure of oxygen is increased from 70 to 150 mTorr, the VAN films reveal narrower BFO pillars embedded in a CeO_2 matrix, as shown in **Figure 7b** (7). Increasing the working pressure directly enhances the growth rate of the films and reduces the lateral feature size of the nanopillars. However, a higher working pressure causes a larger resistance for the plasma generated from the target surface and decreases the kinetic energy of adatoms (7). Overall, the enhanced working pressure results in a smaller feature size of the BFO nanopillars embedded in the CeO_2 matrix. The abovementioned influences of kinetic control are applicable not only to films prepared via PLD but also to ones synthesized by other physical vapor deposition methods (65, 113).

2.5. Self-Templated Growth

The aforementioned in-plane spontaneous ordering phenomenon occurs on untreated, uniform, and atomically flat STO substrates. This section discusses long-range ordering or patterned VAN growth on self-templated substrates with regular chemical, structural, and strain dissimilarities. This type of growth is still classified as spontaneous ordering, since no external masks are involved or removed by this process.

Substrates are not only the mechanical support for thin films, but also the functional entities in thin film technology (3, 114). For epitaxial thin film growth, the substrates usually need to be single crystals with clean, smooth surfaces and uniform chemical terminations at microscopic dimensions. Meanwhile, the intentional surface recrystallization on the substrate surface can be utilized to enable nanoscale tailoring through the trench and terrace structures reconstructed on the surface (66, 115, 116). Self-assembled VAN thin films with long-range ordering can be constructed by selective nucleation and growth on substrates with patterned termination from heat treatment.

A simple heat treatment (e.g., 1,000°C for 1 h) can be used to fabricate alternating SrO and TiO_2 termination strip regions on STO (001) substrates, providing a prerequisite for the selective nucleation and epitaxy VAN growth. The termination-induced ordering procedure is illustrated in **Figure 8a**. Commercially purchased STO (001) substrates were used, which are single crystalline with SrO- and TiO_2 -terminated regions uniformly mixed and randomly distributed on their clean and flat surfaces. After the simple thermal treatment at 1,000°C, the substrate surface recrystallized; the identical chemical termination regions merged together into SrO- and TiO_2 -terminated band regions as trenches and terraces alternately distributed on the substrate surface (**Figure 8b**) (77). The different chemical terminations have distinct heights, surface energies, lattices, and strain states, inducing selective nucleation in the nanocomposite films. A low laser frequency of 1 Hz was applied during the VAN film growth to ensure sufficient diffusion time for the adatoms to reach the energetically favorable nucleation spots on the substrates.

A self-assembled LSMO- CeO_2 VAN thin film with long-range ordering constructed by selective nucleation of heteroepitaxy on a termination-patterned substrate surface is shown in **Figure 8c-f** (77). CeO_2 (011) domains selectively grow on top of the SrO-terminated area. The

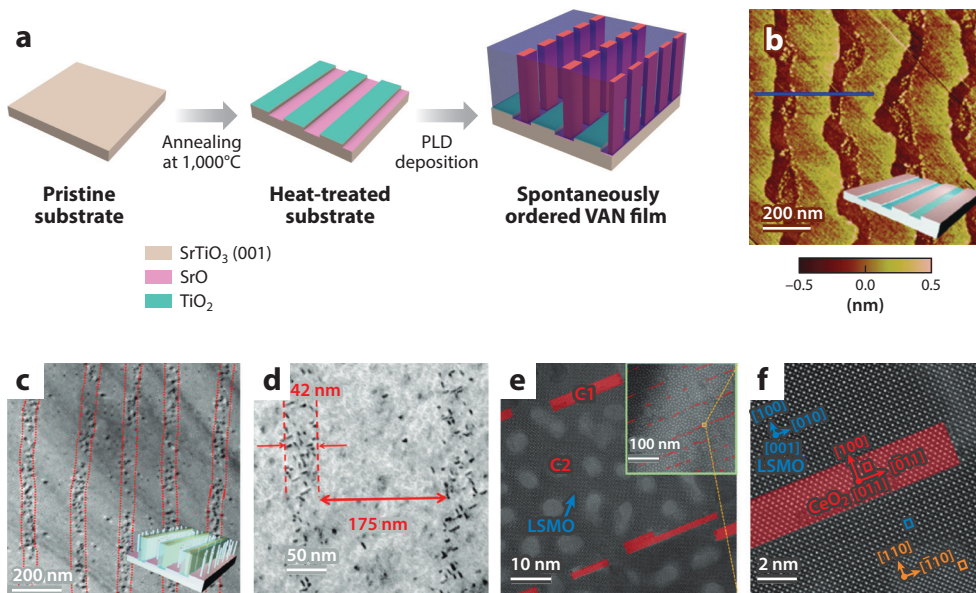


Figure 8

(a) Schematic diagram of the self-templated VAN growth process. (b) AFM topographic image of the heat-treated SrTiO₃ (001) substrate. (c,d) Plan-view TEM images of the LSMO-CeO₂ VAN film grown on a heat-treated substrate, showing spontaneously ordered rectangular CeO₂ nanopillars. Plan-view (e) STEM and (f) HRSTEM images of ordered LSMO-CeO₂ VAN films grown on heat-treated SrTiO₃ substrates with a miscut angle of $\sim 1^\circ$. Abbreviations: AFM, atomic force microscopy; HRSTEM, high-resolution scanning transmission electron microscopy; LSMO, La_{0.7}Sr_{0.3}MnO₃; PLD, pulsed laser deposition; STEM, scanning transmission electron microscopy; TEM, transmission electron microscopy; VAN, vertically aligned nanocomposite. Figure adapted with permission from Reference 77.

in-plane 1D ordered chemical termination nanopattern and selective nucleation induces well-ordered LSMO-CeO₂ VAN thin films with CeO₂ (011) pillars aligned in 1D rectangular domains, embedded in the LSMO matrix, across the entire substrate area. The rectangular CeO₂ nanopillars are selectively grown and confined within the SrO-terminated band region, forming CeO₂ rows in the LSMO matrix (**Figure 8c**). This remarkable selective nucleation of CeO₂ on SrO- and TiO₂-terminated regions could be correlated to the modulated surface energy for SrO and TiO₂ termination of (001) substrates. As shown in **Figure 8d**, the width of the rectangular CeO₂ pillar rows is approximately 42 nm, and the spacing between rows is approximately 175 nm, corresponding to the dimensions of SrO- and TiO₂-terminated regions distributed on the treated substrate surface.

The dimensions of the rectangular CeO₂ pillar rows can easily be tuned by employing substrates with different miscut angles of $\sim 0.17^\circ$, 0.38° , and 1° . For example, the spacing between the CeO₂ pillar rows is tuned to ~ 30 nm when an STO substrate with a miscut angle of $\sim 1^\circ$ is used (**Figure 8e**). The rectangular CeO₂ pillars are well aligned on the SrO-terminated regions. In contrast, the circular CeO₂ nanopillars are disordered on the TiO₂-terminated terraces, similar to those grown on untreated substrates. Not only are the locations and shapes controllable, but the orientations of the CeO₂ nanopillars also can be precisely controlled on different termination regions (**Figure 8f**). Patterned substrates have more flexibility and possibilities by varying the thermal treatment conditions or by combining thermal and chemical treatment, providing promising future potential for nanoscale device integration (115, 117).

In summary, the prepatterned substrate method provides long-range ordering growth for heteroepitaxial VAN thin films and promotes VAN thin film applications to a higher level, closer to future nanoscale device integration. The method can be widely applied to many perovskite substrates, such as STO, LAO, $\text{La}_{0.18}\text{Sr}_{0.82}\text{Al}_{0.59}\text{Ta}_{0.41}\text{O}_3$, YAlO_3 , and NdGaO_3 , to achieve long-range ordering and, hence, patterned VAN growth (117). This is a significant step forward for nanoscale devices with tunable functionalities.

3. OUT-OF-PLANE SPONTANEOUS ORDERING

Until now, we have discussed major approaches and mechanisms for in-plane spontaneous ordering in VAN thin films. Yet, accomplishing out-of-plane spontaneous ordering in VAN films, such as recently reported nanodumbbell structures (22, 118), is also of significance for nanoelectronic devices.

Similar to in-plane ordering, out-of-plane spontaneous ordering is also strongly impacted by strain energy and is achieved by anisotropic in-plane strain fields. This has been confirmed by the self-assembly of bilayer VAN films with one material in common within each layer of the VAN, namely, in the double VAN of YSZ-STO/Sm-doped CeO_2 -STO (119). More recently, out-of-plane ordering has been shown in interlayered VANs, as in **Figure 9a–d** (22). An LSMO- CeO_2 VAN thin film was first deposited on an untreated STO substrate (**Figure 9a, subpanel i**), followed by the deposition of a thin CeO_2 buffer layer that covered the top surface of the first VAN layer (**Figure 9a, subpanel ii**). In contrast to the untreated substrate, the surface of the CeO_2 buffer (or capping) layer is chemically homogeneous but has differently strained regions corresponding to varied in-plane strain fields. The CeO_2 regions on top of LSMO domains are under tension in-plane, while the ones on top of CeO_2 nanopillars are under compression or no strain in-plane. Therefore, when the second LSMO- CeO_2 VAN layer is grown on top of the buffer layer, it exhibits self-assembled CeO_2 nanopillar registration pairing to the CeO_2 nanopillars in the bottom VAN layer (**Figure 9b–d**) (22). This spontaneous out-of-plane ordering is achieved despite the fact that the two VAN layers are separated by the single-phase CeO_2 buffer layer, confirming the key role of strain-driven nucleation and growth. More specifically, the in-plane strain anisotropy drives adatoms to diffuse to the energetically suitable sites, releasing the strain energy and thus leading to the out-of-plane spontaneous ordering. Surface diffusion on the buffer layer (or capping layer) driven by in-plane strain field anisotropy leads to self-organized vertical alignment of domains. By making use of this in-plane strain-driven nucleation mechanism, researchers can purposely design smart materials by stacking nanoparticles, nanopillars, or other shaped domains at specific locations in the matrix according to desired properties and applications. In fact, the vertical ordering or pairing of stacked quantum dots induced by an elastic strain field has been studied in other multilayer systems for semiconductor and optical applications; in these systems, the out-of-plane ordering is consistently driven by the varying in-plane strain fields (12, 111, 120, 121).

Strain-driven vertical ordering has led to the demonstration of coaxial growth of nanodumbbell structures (**Figure 9e–g**) (22). For the LSMO- CeO_2 system, the nanodumbbell structure is constructed through a sequential deposition by alternating two targets, L9C1 and L7C3, in a multilayer fashion. L9C1 and L7C3 are prepared with the same components (LSMO and CeO_2) but with different compositions—the relative ratios are 9:1 and 7:3, respectively. Although the two targets are alternated periodically during the deposition procedure, the nanodumbbell-shaped CeO_2 nanopillars are all coaxially grown and vertically aligned in the LSMO matrix. Overall, the strain effect has a direct and profound influence on registration of the nanodomains during vertical stacking and facilitates out-of-plane spontaneous ordering of the VAN films, which expands the dimension of spontaneous ordering to 3D in VAN films.

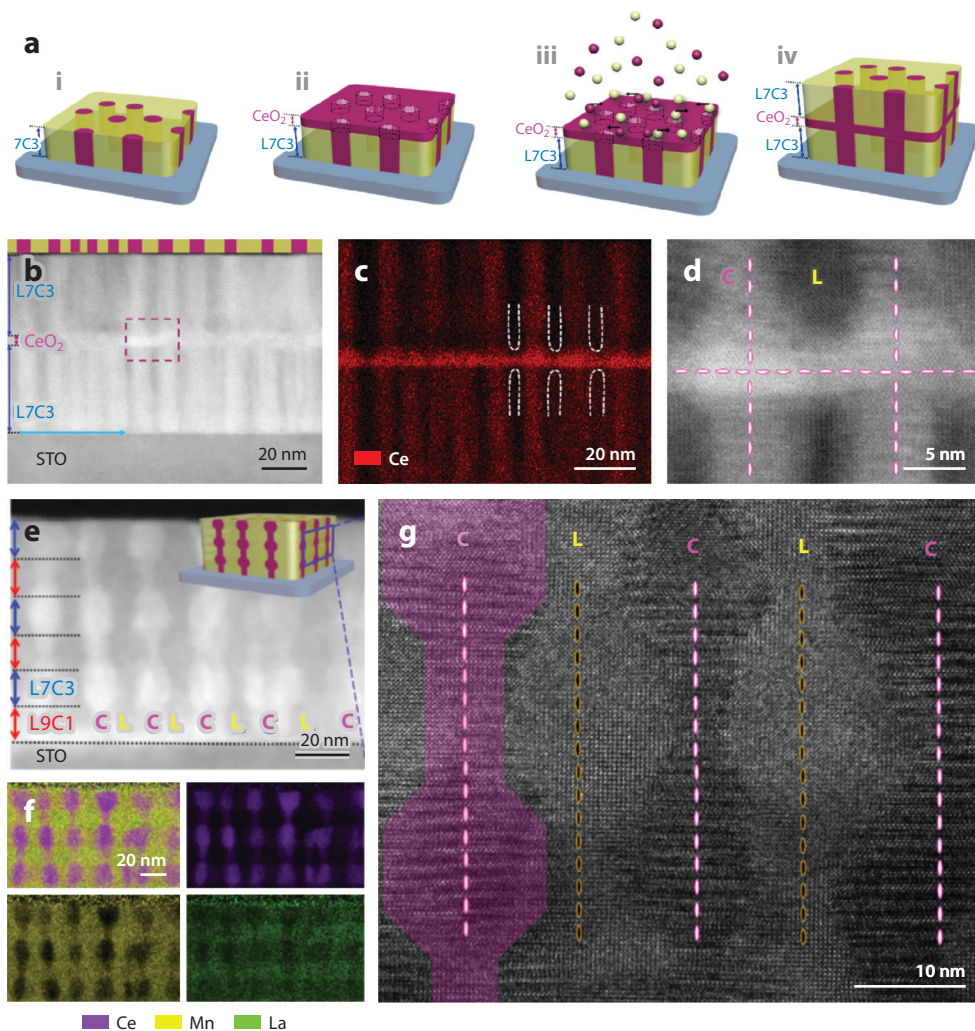


Figure 9

(*a, i-iv*) Schematic diagrams demonstrating the strain-driven growth process of a self-assembled 3D LSMO-CeO₂ framework structure with a thin CeO₂ interlayer. Cross-sectional (*b*) STEM and (*c*) EDS mapping of Ce and (*d*) HRSTEM images of this 3D framework structure showing fine CeO₂ nanopillar registration evenly separated by the interlayer. Cross-sectional (*e*) STEM, (*f*) corresponding EDS mapping, and (*g*) HRTEM images of an LSMO-CeO₂ nanodumbbell structure thin film with the nanodumbbell-shaped CeO₂ nanopillars coaxially and vertically aligned in the LSMO matrix. Abbreviations: C, CeO₂; EDS, energy-dispersive X-ray spectroscopy; HRSTEM, high-resolution scanning transmission electron microscopy; HRTEM, high-resolution transmission electron microscopy; L, La_{0.7}Sr_{0.3}MnO₃; LSMO, La_{0.7}Sr_{0.3}MnO₃; STEM, scanning transmission electron microscopy; STO, SrTiO₃. Figure adapted with permission from Reference 22.

4. ORDERED PLANAR STRUCTURES

Another intriguing type of out-of-plane spontaneous ordering that can be created via one-step PLD from a composite target is a multilayer microstructure with vertically stacked planar domains, such as the reported (YBa₂Cu₃O_{7- δ})_{1-x}-(BaZrO₃)_x epitaxial nanocomposite films (18). A microstructural evolution from vertical pillars to the planar structure is accomplished simply by

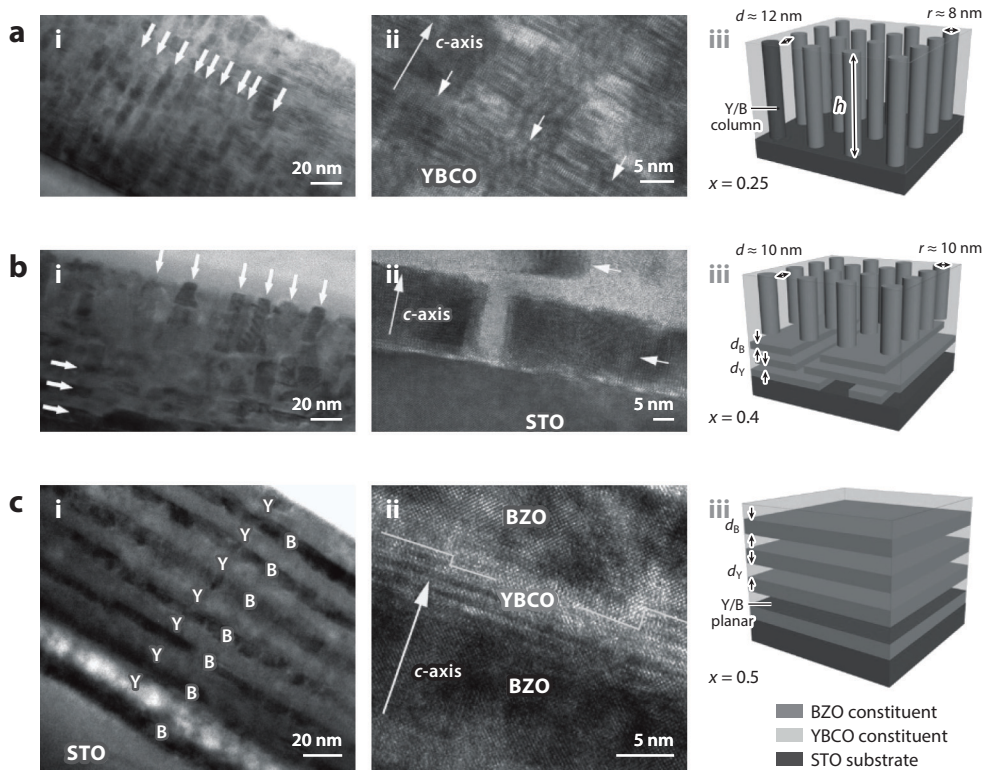


Figure 10

Cross-sectional TEM images of $(\text{YBCO})_{1-x}-(\text{BZO})_x$ epitaxial nanocomposite films with gradually enhanced composition $x = (a)$ 0.25, (b) 0.4, and (c) 0.5. Y and B correspond to YBCO and BZO phases, exhibiting bright and dark contrast in the TEM images, respectively. Each microstructure is illustrated in the schematic diagram at the right, in which Y/B column and Y/B planar represent the vertical and horizontal interfaces between YBCO and BZO. Abbreviations: BZO, BaZrO_3 ; STO, SrTiO_3 ; TEM, transmission electron microscopy; YBCO, $\text{YBa}_2\text{Cu}_3\text{O}_{7-\delta}$. Figure adapted with permission from Reference 18.

increasing x . The switch is related to a release in strain energy, which builds up in $\text{YBa}_2\text{Cu}_3\text{O}_{7-\delta}$ with increasing x as stiffer BZO pillars (hence, more interfaces form and therefore more strain energy).

When $x < 0.4$, BaZrO_3 (BZO) domains are nanocolumnar in shape and vertically aligned in the YBCO matrix (**Figure 10a**) via vertical interfacial coupling. At $x = 0.4$, a microstructural transition occurs with horizontal planar nanodomains stacked on the bottom of the film and vertical columnar nanostructures arranged on the top (**Figure 10b**). The switch from a vertical structure to a horizontal one is abrupt, with the strain-driven interfacial energy minimization being the important factor. BZO is stiff and accordingly inputs strain into YBCO via interfacial coupling. To relieve the large strain energy accumulated, a transformation is needed. At $x = 0.4$, a hybrid vertical and planar structure is achieved, but for $x > 0.5$, instead of VAN, only the planar structure is achieved (**Figure 10c**). Each horizontal planar domain has a similar thickness and is stacked up in a perfect alternate sequence. The YBCO lattice is thus no longer strained. Because of the lack of strain for the planar structure, one might expect it to form no matter the x value. However, this cannot occur because for low x values, the diffusion distances for BZO would be too large to enable the planar structure to form. Thus, both kinetics and thermodynamics (interfacial energies)

play important roles in determining the overall form of the VAN structure. More details on the interfacial strain energy balance are given in Reference 18. Many potential applications requiring the 3D nanoscale engineering described in this section can be envisioned, from superconductor pinning tailored for different applications, to 3D ionic structures for energy storage/generation applications, to memristors with tunable and robust on-off ratios.

5. SUMMARY AND PROSPECTS

Spontaneously, spatially ordered/patterned growth of VAN thin films presented and analyzed in this article offers opportunities both for functional material exploration and next-generation nanoscale devices. Different from templated VAN growth, spontaneous ordering is preferred for device applications. The spontaneous ordering discussed in this review includes both in-plane and out-of-plane spatial ordering.

Spontaneously ordered structures are mainly based on oxide-oxide nanocomposite systems prepared through physical vapor deposition. The strategies and related principles discussed are also applicable to chemical solution synthesis and to oxide-metal and nitride-metal nanocomposite systems (30, 108, 122–125). Success of the strategies requires that metal adatoms easily diffuse on the substrate surface and travel to energetically favorable sites. Some metals can act as catalysts to facilitate the kinetics and hence growth of certain oxides. A recent example uses an Au-BaTiO₃ (BTO) nanostructure to initiate the epitaxial growth of ZnO nanopillars and form arrays of so-called nanoman-like structures as shown in **Figure 11** (123). High tunability of the complex

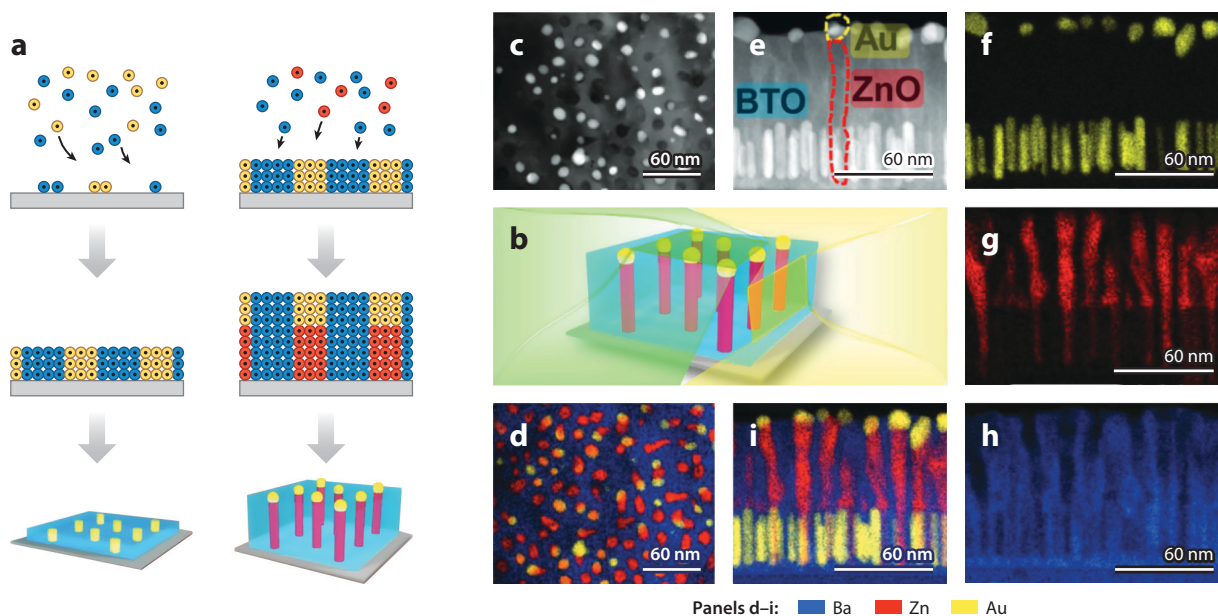


Figure 11

(a) Schematic diagrams showing the two-step growth process of an out-of-plane ordered three-phase Au-BTO-ZnO nanocomposite film. The yellow, blue, and red circles represent the adatoms of Au, BTO, and ZnO, respectively. (b) Three-dimensional schematic microstructure of this Au-BTO-ZnO nanocomposite thin film with out-of-plane ordering. (c) STEM and (d) EDS mapping images showing the plan-view microstructure of this thin film. Cross-sectional (e) STEM and (f–i) EDS mapping images showing the out-of-plane ordered microstructure. Abbreviations: BTO, BaTiO₃; EDS, energy-dispersive X-ray spectroscopy; HAADF, high-angle annular dark-field; STEM, scanning transmission electron microscopy. Figure adapted with permission from Reference 123.

dielectric function and hyperbolic optical properties demonstrated in the ordered Au-BTO-ZnO system demonstrates the power of the ordering approach in optical property control. Overall, spontaneously ordered oxide-oxide and oxide-metal nanocomposites (104, 126, 127) offer a unique design space for oxide-based functional systems for future novel functionalities and multifunctionalities, in the realm of both basic science understanding and novel device engineering.

DISCLOSURE STATEMENT

The authors are not aware of any affiliations, memberships, funding, or financial holdings that might be perceived as affecting the objectivity of this review.

ACKNOWLEDGMENTS

The US–UK collaborative effort was funded by the US National Science Foundation (ECCS-1902644 and ECCS-1902623) and by Engineering and Physical Sciences Research Council (EPSRC) grant EP/T012218/1. X.S. and H.W. acknowledge support from the US National Science Foundation (DMR-1565822 and DMR-1809520). J.L.M.-D. acknowledges support from Leverhulme Trust grant RPG-2015-017, EPSRC grants EP/N004272/1 and EP/M000524/1, and Royal Academy of Engineering grant CIET1819_24.

LITERATURE CITED

1. Hwang J, Feng Z, Charles N, Wang XR, Lee D, et al. 2019. Tuning perovskite oxides by strain: electronic structure, properties, and functions in (electro)catalysis and ferroelectricity. *Mater. Today* 31:100–18
2. Bhalla AS, Guo RY, Roy R. 2000. The perovskite structure—a review of its role in ceramic science and technology. *Mater. Res. Innov.* 4:3–26
3. Habermeyer HU. 2007. Thin films of perovskite-type complex oxides. *Mater. Today* 10:34–43
4. Martin LW, Chu YH, Ramesh R. 2010. Advances in the growth and characterization of magnetic, ferroelectric, and multiferroic oxide thin films. *Mat. Sci. Eng. R Rep.* 68:89–133
5. Ramesh R, Schlom DG. 2019. Creating emergent phenomena in oxide superlattices. *Nat. Rev. Mater.* 4:257–68
6. Vrejoiu I, Alexe M, Hesse D, Gosele U. 2008. Functional perovskites—from epitaxial films to nanostructured arrays. *Adv. Funct. Mater.* 18:3892–906
7. Jiang J, Yang Q, Zhang Y, Li XY, Shao PW, et al. 2019. Self-assembled ferroelectric nanoarray. *ACS Appl. Mater. Interfaces* 11:2205–10
8. Zhang WR, Chen AP, Bi ZK, Jia QX, MacManus-Driscoll JL, Wang HY. 2014. Interfacial coupling in heteroepitaxial vertically aligned nanocomposite thin films: from lateral to vertical control. *Curr. Opin. Solid State Mater. Sci.* 18:6–18
9. MacManus-Driscoll JL, Suwardi A, Wang H. 2015. Composite epitaxial thin films: a new platform for tuning, probing, and exploiting mesoscale oxides. *MRS Bull.* 40:933–42
10. Huang JJ, MacManus-Driscoll JL, Wang HY. 2017. New epitaxy paradigm in epitaxial self-assembled oxide vertically aligned nanocomposite thin films. *J. Mater. Res.* 32:4054–66
11. Chen AP, Bi ZX, Jia QX, MacManus-Driscoll JL, Wang HY. 2013. Microstructure, vertical strain control and tunable functionalities in self-assembled, vertically aligned nanocomposite thin films. *Acta Mater.* 61:2783–92
12. MacManus-Driscoll JL. 2010. Self-assembled heteroepitaxial oxide nanocomposite thin film structures: designing interface-induced functionality in electronic materials. *Adv. Funct. Mater.* 20:2035–45
13. MacManus-Driscoll JL, Zerrer P, Wang HY, Yang H, Yoon J, et al. 2008. Strain control and spontaneous phase ordering in vertical nanocomposite heteroepitaxial thin films. *Nat. Mater.* 7:314–20
14. Zhang WR, Ramesh R, MacManus-Driscoll JL, Wang HY. 2015. Multifunctional, self-assembled oxide nanocomposite thin films and devices. *MRS Bull.* 40:736–45

15. Chen A, Su Q, Han H, Enriquez E, Jia Q. Metal oxide nanocomposites: a perspective from strain, defect, and interface. *Adv. Mater.* 31:1803241
16. MacManus-Driscoll J, Suardi A, Kursumovic A, Bi ZX, Tsai CF, et al. 2015. New strain states and radical property tuning of metal oxides using a nanocomposite thin film approach. *APL Mater.* 3:062507
17. Yang H, Wang HY, Yoon J, Wang YQ, Jain M, et al. 2009. Vertical interface effect on the physical properties of self-assembled nanocomposite epitaxial films. *Adv. Mater.* 21:3794–98
18. Zhao R, Li WW, Lee JH, Choi EM, Liang Y, et al. 2014. Precise tuning of $(\text{YBa}_2\text{Cu}_3\text{O}_{7-\delta})_{1-x}:(\text{BaZrO}_3)_x$ thin film nanocomposite structures. *Adv. Funct. Mater.* 24:5240–45
19. Harrington SA, Zhai JY, Denev S, Gopalan V, Wang HY, et al. 2011. Thick lead-free ferroelectric films with high Curie temperatures through nanocomposite-induced strain. *Nat. Nanotechnol.* 6:491–95
20. Zhan Q, Yu R, Crane SP, Zheng H, Kisielowski C, Ramesh R. 2006. Structure and interface chemistry of perovskite-spinel nanocomposite thin films. *Appl. Phys. Lett.* 89:172902
21. Sun X, Li Q, Huang J, Jian J, Lu P, et al. 2019. Strain and property tuning of the 3D framed epitaxial nanocomposite thin films via interlayer thickness variation. *J. Appl. Phys.* 125:082530
22. Sun X, Li Q, Huang J, Fan M, Rutherford BX, et al. 2019. Strain-driven nanodumbbell structure and enhanced physical properties in hybrid vertically aligned nanocomposite thin films. *Appl. Mater. Today* 16:204–12
23. Chen AP, Bi ZX, Tsai CF, Lee J, Su Q, et al. 2011. Tunable low-field magnetoresistance in $(\text{La}_{0.7}\text{Sr}_{0.3}\text{MnO}_3)_{0.5}:(\text{ZnO})_{0.5}$ self-assembled vertically aligned nanocomposite thin films. *Adv. Funct. Mater.* 21:2423–29
24. Gao XY, Li LG, Jian J, Huang JJ, Sun X, et al. 2019. Tunable low-field magnetoresistance properties in $(\text{La}_{0.7}\text{Ca}_{0.3}\text{MnO}_3)_{1-x}:(\text{CeO}_2)_x$ vertically aligned nanocomposite thin films. *Appl. Phys. Lett.* 115:053103
25. Choi EM, Di Bernardo A, Zhu BN, Lu P, Alpern H, et al. 2019. 3D strain-induced superconductivity in $\text{La}_2\text{CuO}_{4+\delta}$ using a simple vertically aligned nanocomposite approach. *Sci. Adv.* 5:eav5532
26. Fan M, Wang H, Misra S, Zhang B, Qi ZM, et al. 2018. Microstructure, magnetic, and magnetoresistance properties of $\text{La}_{0.7}\text{Sr}_{0.3}\text{MnO}_3:\text{CuO}$ nanocomposite thin films. *ACS Appl. Mater. Interfaces* 10:5779–84
27. Sun X, Huang JJ, Jian J, Fan M, Wang H, et al. 2018. Three-dimensional strain engineering in epitaxial vertically aligned nanocomposite thin films with tunable magnetotransport properties. *Mater. Horiz.* 5:536–44
28. Huang JJ, Gellatly A, Kauffmann A, Sun X, Wang HY. 2018. Exchange bias effect along vertical interfaces in $\text{La}_{0.7}\text{Sr}_{0.3}\text{MnO}_3:\text{NiO}$ vertically aligned nanocomposite thin films integrated on silicon substrates. *Cryst. Growth Des.* 18:4388–94
29. Huang JJ, Jin TN, Misra S, Wang H, Qi ZM, et al. 2018. Tailorable optical response of $\text{Au}-\text{LiNbO}_3$ hybrid metamaterial thin films for optical waveguide applications. *Adv. Opt. Mater.* 6:1800510
30. Huang JJ, Li LG, Lu P, Qi ZM, Sun X, et al. 2017. Self-assembled $\text{Co}-\text{BaZrO}_3$ nanocomposite thin films with ultra-fine vertically aligned Co nanopillars. *Nanoscale* 9:7970–76
31. Wang H, Li LG, Huang JJ, Gao XY, Sun X, et al. 2019. Two-phase room-temperature multiferroic nanocomposite with BiMnO_3 -tilted nanopillars in the $\text{Bi}_2\text{W}_{1-x}\text{Mn}_x\text{O}_6$ matrix. *ACS Appl. Mater. Interfaces* 11:26261–67
32. Wang H, Li L, Huang J, Gao X, Sun X, Wang H. 2019. Multiferroic vertically aligned nanocomposite with CoFe_2O_4 nanocones embedded in layered Bi_2WO_6 matrix. *Mater. Res. Lett.* 7:418–25
33. Bhushan B, Jung YC. 2011. Natural and biomimetic artificial surfaces for superhydrophobicity, self-cleaning, low adhesion, and drag reduction. *Prog. Mater. Sci.* 56:1–108
34. Liu KS, Jiang L. 2012. Bio-inspired self-cleaning surfaces. *Annu. Rev. Mater. Res.* 42:231–63
35. Wang ST, Liu KS, Yao X, Jiang L. 2015. Bioinspired surfaces with superwettability: new insight on theory, design, and applications. *Chem. Rev.* 115:8230–93
36. Chen K, Li L. 2019. Ordered structures with functional units as a paradigm of material design. *Adv. Mater.* 31:1901115
37. Teyssier J, Saenko SV, van der Marel D, Milinkovitch MC. 2015. Photonic crystals cause active colour change in chameleons. *Nat. Commun.* 6:6368
38. Bae WG, Kim HN, Kim D, Park SH, Jeong HE, Suh KY. 2014. 25th anniversary article: scalable multiscale patterned structures inspired by nature: the role of hierarchy. *Adv. Mater.* 26:675–700

39. Sun MH, Huang SZ, Chen LH, Li Y, Yang XY, et al. 2016. Applications of hierarchically structured porous materials from energy storage and conversion, catalysis, photocatalysis, adsorption, separation, and sensing to biomedicine. *Chem. Soc. Rev.* 45:3479–563
40. Gogolides E, Ellinas K, Tserpi A. 2015. Hierarchical micro and nano structured, hydrophilic, superhydrophobic and superoleophobic surfaces incorporated in microfluidics, microarrays and lab on chip microsystems. *Microelectron. Eng.* 132:135–55
41. Dumanli AG, Savin T. 2016. Recent advances in the biomimicry of structural colours. *Chem. Soc. Rev.* 45:6698–724
42. Phillips KR, England GT, Sunny S, Shirman E, Shirman T, et al. 2016. A colloidoscope of colloid-based porous materials and their uses. *Chem. Soc. Rev.* 45:281–322
43. Chen HY, Brivio S, Chang CC, Frascaroli J, Hou TH, et al. 2017. Resistive random access memory (RRAM) technology: from material, device, selector, 3D integration to bottom-up fabrication. *J. Electroceramics* 39:21–38
44. Jones MR, Osberg KD, Macfarlane RJ, Langille MR, Mirkin CA. 2011. Templated techniques for the synthesis and assembly of plasmonic nanostructures. *Chem. Rev.* 111:3736–827
45. Cummins C, Ghoshal T, Holmes JD, Morris MA. 2016. Strategies for inorganic incorporation using neat block copolymer thin films for etch mask function and nanotechnological application. *Adv. Mater.* 28:5586–618
46. Jeong SJ, Kim JY, Kim BH, Moon HS, Kim SO. 2013. Directed self-assembly of block copolymers for next generation nanolithography. *Mater. Today* 16:468–76
47. Lotito V, Zambelli T. 2017. Approaches to self-assembly of colloidal monolayers: a guide for nanotechnologists. *Adv. Colloid Interface Sci.* 246:217–74
48. Zadin V, Brandell D, Kasemagi H, Aabloo A, Thomas JO. 2011. Finite element modelling of ion transport in the electrolyte of a 3D-microbattery. *Solid State Ionics* 192:279–83
49. van Dommelen R, Fanzio P, Sasso L. 2018. Surface self-assembly of colloidal crystals for micro- and nano-patterning. *Adv. Colloid Interface Sci.* 251:97–114
50. Hwang HY, Palstra TTM, Cheong SW, Batlogg B. 1995. Pressure effects on the magnetoresistance in doped manganese perovskites. *Phys. Rev. B* 52:15046
51. Choi HK, Aimon NM, Kim DH, Sun XY, Gwyther J, et al. 2014. Hierarchical templating of a BiFeO₃–CoFe₂O₄ multiferroic nanocomposite by a triblock terpolymer film. *ACS Nano* 8:9248–54
52. Kim DH, Ning S, Ross CA. 2019. Self-assembled multiferroic perovskite–spinel nanocomposite thin films: epitaxial growth, templating and integration on silicon. *J. Mater. Chem. C* 7:9128–48
53. Comes R, Liu HX, Kholchov M, Kasica R, Lu JW, Wolf SA. 2012. Directed self-assembly of epitaxial CoFe₂O₄–BiFeO₃ multiferroic nanocomposites. *Nano Lett.* 12:2367–73
54. Ni JF, Li L. 2018. Self-supported 3D array electrodes for sodium microbatteries. *Adv. Funct. Mater.* 28:1704880
55. Arthur TS, Bates DJ, Cirigliano N, Johnson DC, Malati P, et al. 2011. Three-dimensional electrodes and battery architectures. *MRS Bull.* 36:523–31
56. Reddy ALM, Gowda SR, Shaijumon MM, Ajayan PM. 2012. Hybrid nanostructures for energy storage applications. *Adv. Mater.* 24:5045–64
57. Zhang F, Qi LM. 2016. Recent progress in self-supported metal oxide nanoarray electrodes for advanced lithium-ion batteries. *Adv. Sci.* 3:1600049
58. Chen Y, Pepin A. 2001. Nanofabrication: conventional and nonconventional methods. *Electrohoresis* 22:187–207
59. Barth JV, Costantini G, Kern K. 2005. Engineering atomic and molecular nanostructures at surfaces. *Nature* 437:671–79
60. Skolnick MS, Mowbray DJ. 2004. Self-assembled semiconductor quantum dots: fundamental physics and device applications. *Annu. Rev. Mater. Res.* 34:181–218
61. Scott JF. 2007. Applications of modern ferroelectrics. *Science* 315:954–59
62. Pauzauskie PJ, Yang P. 2006. Nanowire photonics. *Mater. Today* 9:36–45
63. Lee S, MacManus-Driscoll JL. 2017. Research update: fast and tunable nanoionics in vertically aligned nanostructured films. *APL Mater.* 5:042304

64. Zheng H, Zhan Q, Zavaliche F, Sherburne M, Straub F, et al. 2006. Controlling self-assembled perovskite-spinel nanostructures. *Nano Lett.* 6:1401–7
65. Kim TC, Lee SH, Jung HK, Kim YE, Choi JW, et al. 2019. Effect of sputtering conditions on the structure and magnetic properties of self-assembled BiFeO₃-CoFe₂O₄ nanocomposite thin films. *J. Magn. Mater.* 471:116–23
66. Obradors X, Puig T, Gibert M, Queralto A, Zabaleta J, Mestres N. 2014. Chemical solution route to self-assembled epitaxial oxide nanostructures. *Chem. Soc. Rev.* 43:2200–25
67. Schlom DG, Chen LQ, Pan XQ, Schmehl A, Zurbuchen MA. 2008. A thin film approach to engineering functionality into oxides. *J. Am. Ceram. Soc.* 91:2429–54
68. Chambers SA. 2010. Epitaxial growth and properties of doped transition metal and complex oxide films. *Adv. Mater.* 22:219–48
69. Martin LW, Schlom DG. 2012. Advanced synthesis techniques and routes to new single-phase multiferroics. *Curr. Opin. Solid State Mater. Sci.* 16:199–215
70. Blamire MG, MacManus-Driscoll JL, Mathur ND, Barber ZH. 2009. The materials science of functional oxide thin films. *Adv. Mater.* 21:3827–39
71. Zou GF, Zhao J, Luo HM, McCleskey TM, Burrell AK, Jia QX. 2013. Polymer-assisted-deposition: a chemical solution route for a wide range of materials. *Chem. Soc. Rev.* 42:439–49
72. Brune H, Giovannini M, Bromann K, Kern K. 1998. Self-organized growth of nanostructure arrays on strain-relief patterns. *Nature* 394:451–53
73. Zhang WR, Li LG, Lu P, Fan M, Su Q, et al. 2015. Perpendicular exchange-biased magnetotransport at the vertical heterointerfaces in La_{0.7}Sr_{0.3}MnO₃:NiO nanocomposites. *ACS Appl. Mater. Interfaces* 7:21646–51
74. Wang ZG, Li YX, Viswan R, Hu BL, Harris VG, et al. 2013. Engineered magnetic shape anisotropy in BiFeO₃-CoFe₂O₄ self-assembled thin films. *ACS Nano* 7:3447–56
75. Zheng HM, Straub F, Zhan Q, Yang PL, Hsieh WK, et al. 2006. Self-assembled growth of BiFeO₃-CoFe₂O₄ nanostructures. *Adv. Mater.* 18:2747–52
76. Dix N, Muralidharan R, Warot-Fonrose B, Varela M, Sanchez F, Fontcuberta J. 2009. Critical limitations in the fabrication of biferroic BiFeO₃-CoFe₂O₄ columnar nanocomposites due to bismuth loss. *Chem. Mater.* 21:1375–80
77. Fan M, Zhang B, Wang H, Jian J, Sun X, et al. 2017. Self-organized epitaxial vertically aligned nanocomposites with long-range ordering enabled by substrate nanotemplating. *Adv. Mater.* 29:1606861
78. Biswas A, Rossen PB, Yang CH, Siemons W, Jung MH, et al. 2011. Universal Ti-rich termination of atomically flat SrTiO₃ (001), (110), and (111) surfaces. *Appl. Phys. Lett.* 98:051904
79. Woo S, Jeong H, Lee SA, Seo H, Lacotte M, et al. 2015. Surface properties of atomically flat polycrystalline SrTiO₃. *Sci. Rep.* 5:8822
80. Zhang KHL, Walsh A, Catlow CRA, Lazarov VK, Egdell RG. 2010. Surface energies control the self-organization of oriented In₂O₃ nanostructures on cubic zirconia. *Nano Lett.* 10:3740–46
81. Yan L, Bai FM, Li JF, Viehland D. 2009. Nanobelt structure in perovskite-spinel composite thin films. *J. Am. Ceram. Soc.* 92:17–20
82. Yan L, Yang YD, Wang ZG, Xing ZP, Li JF, Viehland D. 2009. Review of magnetoelectric perovskite-spinel self-assembled nano-composite thin films. *J. Mater. Sci.* 44:5080–94
83. Kim DH, Sun XY, Aimon NM, Kim JJ, Campion MJ, et al. 2015. A three component self-assembled epitaxial nanocomposite thin film. *Adv. Funct. Mater.* 25:3091–100
84. Zhong GK, An F, Bitla Y, Wang JB, Zhong XL, et al. 2018. Self-assembling epitaxial growth of a single crystalline CoFe₂O₄ nanopillar array via dual-target pulsed laser deposition. *J. Mater. Chem. C* 6:4854–60
85. Takahashi R, Misumi H, Yamamoto T, Lippmaa M. 2014. Spontaneous growth of strain-free magnetite nanocrystals via temperature-driven dewetting. *Cryst. Growth Des.* 14:1264–71
86. Slutsker J, Levin I, Li JH, Artemev A, Roytburd AL. 2006. Effect of elastic interactions on the self-assembly of multiferroic nanostructures in epitaxial films. *Phys. Rev. B* 73:184127
87. Levin I, Li JH, Slutsker J, Roytburd AL. 2006. Design of self-assembled multiferroic nanostructures in epitaxial films. *Adv. Mater.* 18:2044–47
88. Dawber M, Szafraniak I, Alexe M, Scott JF. 2003. Self-patterning of arrays of ferroelectric capacitors: description by theory of substrate mediated strain interactions. *J. Phys. Condens. Matter* 15:L667–71

89. Chambliss DD, Wilson RJ, Chiang S. 1991. Nucleation of ordered Ni island arrays on Au(111) by surface-lattice dislocations. *Phys. Rev. Lett.* 66:1721–24
90. Nilius N, Rienks EDL, Rust HP, Freund HJ. 2005. Self-organization of gold atoms on a polar FeO(111) surface. *Phys. Rev. Lett.* 95:066101
91. Shchukin VA, Bimberg D. 1999. Spontaneous ordering of nanostructures on crystal surfaces. *Rev. Mod. Phys.* 71:1125–71
92. Schlom DG, Chen LQ, Eom CB, Rabe KM, Streiffer SK, Triscone JM. 2007. Strain tuning of ferroelectric thin films. *Annu. Rev. Mater. Res.* 37:589–626
93. Liao SC, Tsai PY, Liang CW, Liu HJ, Yang JC, et al. 2011. Misorientation control and functionality design of nanopillars in self-assembled perovskite-spinel heteroepitaxial nanostructures. *ACS Nano* 5:4118–22
94. Dix N, Muralidharan R, Rebled JM, Estrade S, Peiro F, et al. 2010. Selectable spontaneous polarization direction and magnetic anisotropy in BiFeO₃–CoFe₂O₄ epitaxial nanostructures. *ACS Nano* 4:4955–61
95. Chen AP, Weigand M, Bi ZX, Zhang WR, Lu XJ, et al. 2014. Evolution of microstructure, strain and physical properties in oxide nanocomposite films. *Sci. Rep.* 4:5426
96. Zhu YM, Liu PP, Yu R, Hsieh YH, Ke D, et al. 2014. Orientation-tuning in self-assembled heterostructures induced by a buffer layer. *Nanoscale* 6:5126–31
97. Crane SP, Bihler C, Brandt MS, Goennenwein STB, Gajek M, Ramesh R. 2009. Tuning magnetic properties of magnetoelectric BiFeO₃–NiFe₂O₄ nanostructures. *J. Magn. Magn. Mater.* 321:L5–L9
98. Bi Z, Lee JH, Yang H, Jia Q, MacManus-Driscoll JL, Wang H. 2009. Tunable lattice strain in vertically aligned nanocomposite (BiFeO₃)_x:(Sm₂O₃)_{1-x} thin films. *J. Appl. Phys.* 106:094309
99. Su Q, Yoon D, Chen AP, Khatkhatay F, Manthiram A, Wang HY. 2013. Vertically aligned nanocomposite electrolytes with superior out-of-plane ionic conductivity for solid oxide fuel cells. *J. Power Sources* 242:455–63
100. Kim DH, Sun X, Kim TC, Eun YJ, Lee T, et al. 2016. Magnetic phase formation in self-assembled epitaxial BiFeO₃–MgO and BiFeO₃–MgAl₂O₄ nanocomposite films grown by combinatorial pulsed laser deposition. *ACS Appl. Mater. Interfaces* 8:2673–79
101. Hsieh YH, Liou JM, Huang BC, Liang CW, He Q, et al. 2012. Local conduction at the BiFeO₃–CoFe₂O₄ tubular oxide interface. *Adv. Mater.* 24:4564–68
102. Fouchet A, Wang HY, Yang H, Yoon J, Jia QX, MacManus-Driscoll JL. 2009. Spontaneous ordering, strain control, and multifunctionality in vertical nanocomposite heteroepitaxial films. *IEEE Trans. Ultrason. Ferroelectr. Freq. Control* 56:1534–38
103. Liu HJ, Liu YY, Tsai CY, Liao SC, Chen YJ, et al. 2015. Tuning the functionalities of a mesocrystal via structural coupling. *Sci. Rep.* 5:12073
104. Huang JJ, Wang XJ, Hogan NL, Wu SX, Lu P, et al. 2018. Nanoscale artificial plasmonic lattice in self-assembled vertically aligned nitride-metal hybrid metamaterials. *Adv. Sci.* 5:1800416
105. Aggarwal S, Monga AP, Perusse SR, Ramesh R, Ballarotto V, et al. 2000. Spontaneous ordering of oxide nanostructures. *Science* 287:2235–37
106. Shchukin VA, Ledentsov NN, Kopev PS, Bimberg D. 1995. Spontaneous ordering of arrays of coherent strained islands. *Phys. Rev. Lett.* 75:2968–71
107. Tersoff J, LeGoues FK. 1994. Competing relaxation mechanisms in strained layers. *Phys. Rev. Lett.* 72:3570–73
108. Su Q, Zhang W, Lu P, Fang S, Khatkhatay F, et al. 2016. Self-assembled magnetic metallic nanopillars in ceramic matrix with anisotropic magnetic and electrical transport properties. *ACS Appl. Mater. Interfaces* 8:20283–91
109. Zheng H, Wang J, Mohaddes-Ardabili L, Wuttig M, Salamanca-Riba L, et al. 2004. Three-dimensional heteroepitaxy in self-assembled BaTiO₃–CoFe₂O₄ nanostructures. *Appl. Phys. Lett.* 85:2035–37
110. Yan L, Bai FM, Li JF, Viehland D. 2010. Nanostructures in perovskite-ferrite two-phase composite epitaxial thin films. *Philos. Mag.* 90:103–11
111. Li XL, Wang CX, Yang GW. 2014. Thermodynamic theory of growth of nanostructures. *Prog. Mater. Sci.* 64:121–99
112. Misra S, Li LG, Jian J, Huang JJ, Wang XJ, et al. 2018. Tailorable Au nanoparticles embedded in epitaxial TiO₂ thin films for tunable optical properties. *ACS Appl. Mater. Interfaces* 10:32895–902

113. Stroschio JA, Pierce DT. 1994. Scaling of diffusion-mediated island growth in iron-on-iron homoepitaxy. *Phys. Rev. B* 49:8522–25
114. Yu P, Chu YH, Ramesh R. 2012. Oxide interfaces: pathways to novel phenomena. *Mater. Today* 15:320–27
115. Sanchez F, Ocal C, Fontcuberta J. 2014. Tailored surfaces of perovskite oxide substrates for conducted growth of thin films. *Chem. Soc. Rev.* 43:2272–85
116. Gibert M, Puig T, Obradors X, Benedetti A, Sandiumenge F, Huhne R. 2007. Self-organization of heteroepitaxial CeO₂ nanodots grown from chemical solutions. *Adv. Mater.* 19:3937–42
117. Biswas A, Yang CH, Ramesh R, Jeong MH. 2017. Atomically flat single terminated oxide substrate surfaces. *Prog. Surf. Sci.* 92:117–41
118. Rizzo F, Augieri A, Armenio AA, Galluzzi V, Mancini A, et al. 2016. Enhanced 77 K vortex-pinning in Y Ba₂Cu₃O_{7-x} films with Ba₂Y TaO₆ and mixed Ba₂Y TaO₆ + Ba₂Y NbO₆ nano-columnar inclusions with irreversibility field to 11 T. *APL Mater.* 4:061101
119. Lee S, Zhang WR, Khatkhatay F, Wang HY, Jia QX, MacManus-Driscoll JL. 2015. Ionic conductivity increased by two orders of magnitude in micrometer-thick vertical yttria-stabilized ZrO₂ nanocomposite films. *Nano Lett.* 15:7362–69
120. Xie QH, Madhukar A, Chen P, Kobayashi NP. 1995. Vertically self-organized InAs quantum box islands on GaAs(100). *Phys. Rev. Lett.* 75:2542–45
121. Schmidt OG, Jin-Phillipp NY, Lange C, Denker U, Eberl K, et al. 2000. Long-range ordered lines of self-assembled Ge islands on a flat Si (001) surface. *Appl. Phys. Lett.* 77:4139–41
122. Huang J, Wang X, Phuah XL, Lu P, Qi Z, Wang H. 2019. Plasmonic Cu nanostructures in ZnO as hyperbolic metamaterial thin films. *Mater. Today Nano* 8:100052
123. Misra S, Li LG, Zhang D, Jian J, Qi ZM, et al. 2019. Self-assembled ordered three-phase Au–BaTiO₃–ZnO vertically aligned nanocomposites achieved by a templating method. *Adv. Mater.* 31:1806529
124. Li LG, Sun LY, Gomez-Diaz JS, Hogan NL, Lu P, et al. 2016. Self-assembled epitaxial Au-oxide vertically aligned nanocomposites for nanoscale metamaterials. *Nano Lett.* 16:3936–43
125. Zhang B, Fan M, Li LG, Jian J, Huang JJ, et al. 2018. Tunable magnetic anisotropy of self-assembled Fe nanostructures within a La_{0.5}Sr_{0.5}FeO₃ matrix. *Appl. Phys. Lett.* 112:013104
126. Wang XJ, Jian J, Zhou ZG, Fan CC, Dai YM, et al. 2019. Self-assembled Ag-TiN hybrid plasmonic metamaterial: tailorable tilted nanopillar and optical properties. *Adv. Opt. Mater.* 7:1801180
127. Wang XJ, Jian J, Diaz-Amaya S, Kumah CE, Lu P, et al. 2019. Hybrid plasmonic Au-TiN vertically aligned nanocomposites: a nanoscale platform towards tunable optical sensing. *Nanoscale Adv.* 1:1045–54

Contents

Data-Driven Discovery of Materials

- Evolving the Materials Genome: How Machine Learning Is Fueling
the Next Generation of Materials Discovery
Changwon Sub, Clyde Fare, James A. Warren, and Edward O. Pyzer-Knapp 1
- Machine Learning for Structural Materials
*Taylor D. Sparks, Steven K. Kauwe, Marcus E. Parry, Aria Mansouri Tehrani,
and Jakoab Brgoch* 27
- Machine Learning in Materials Discovery: Confirmed Predictions
and Their Underlying Approaches
James E. Saal, Anton O. Oliynyk, and Bryce Meredig 49
- Opportunities and Challenges for Machine Learning in Materials
Science
Dane Morgan and Ryan Jacobs 71

Quantum Materials and Devices

- Microwave Microscopy and Its Applications
Zhaodong Chu, Lu Zheng, and Keji Lai 105
- Angle-Resolved Photoemission Spectroscopy Study of Topological
Quantum Materials
Chaofan Zhang, Yiwei Li, Ding Pei, Zhongkai Liu, and Yulin Chen 131
- Epitaxial Growth of Two-Dimensional Layered Transition Metal
Dichalcogenides
*Tanushree H. Choudbury, Xiaotian Zhang, Zakaria Y. Al Balushi,
Mikhail Chubarov, and Joan M. Redwing* 155

Current Interest

- Morphology-Related Functionality in Nanoarchitected GaN
Abhijit Chatterjee, Shashidhara Acharya, and S.M. Shivaprasad 179
- Multiscale Patterning from Competing Interactions and Length Scales
A.R. Bishop 207

Spontaneous Ordering of Oxide-Oxide Epitaxial Vertically Aligned Nanocomposite Thin Films <i>Xing Sun, Judith L. MacManus-Driscoll, and Haiyan Wang</i>	229
Antisymmetry: Fundamentals and Applications <i>Hari Padmanabhan, Jason M. Munro, Ismaila Dabo, and Venkatraman Gopalan</i>	255
Energy Conversion by Phase Transformation in the Small-Temperature-Difference Regime <i>Ashley N. Bucsek, William Nunn, Bharat Jalan, and Richard D. James</i>	283
Hybrid Thermoelectrics <i>Jia Liang, Shujia Yin, and Chunlei Wan</i>	319
Noble Metal Nanomaterials with Nontraditional Crystal Structures <i>Chaitali Sow, Suchithra P, Gangaiab Mettela, and Giridhar U. Kulkarni</i>	345
Muon Spectroscopy for Investigating Diffusion in Energy Storage Materials <i>Innes McClelland, Beth Johnston, Peter J. Baker, Marco Amores, Edmund J. Cussen, and Serena A. Corr</i>	371
High-Energy X-Ray Diffraction Microscopy in Materials Science <i>Joel V. Bernier, Robert M. Suter, Anthony D. Rollett, and Jonathan D. Almer</i>	395
Frontiers in the Simulation of Dislocations <i>Nicolas Bertin, Ryan B. Sills, and Wei Cai</i>	437
Grain Boundary Complexion Transitions <i>Patrick R. Cantwell, Timofey Frolov, Timothy J. Rupert, Amanda R. Krause, Christopher J. Marvel, Gregory S. Rohrer, Jeffrey M. Rickman, and Martin P. Harmer</i>	465
Recent Advances in Solid-State Nuclear Magnetic Resonance Techniques for Materials Research <i>Po-Hsiu Chien, Kent J. Griffith, Haoyu Liu, Zhehong Gan, and Yan-Yan Hu</i>	493
Self-Assembly of Block Copolymers with Tailored Functionality: From the Perspective of Intermolecular Interactions <i>Rui-Yang Wang and Moon Jeong Park</i>	521
Thermoelectric Properties of Semiconducting Polymers <i>Kelly A. Peterson, Elayne M. Thomas, and Michael L. Chabinyc</i>	551
Indexes	
Cumulative Index of Contributing Authors, Volumes 46–50	575

Errata

An online log of corrections to *Annual Review of Materials Research* articles may be found at <http://www.annualreviews.org/errata/matsci>